

# Medium resolution near-infrared spectroscopy of Massive Young Stellar Objects

R. Pomohaci\*, R. D. Oudmaijer, S. L. Lumsden, M. G. Hoare and I. Mendigutía

*School of Physics and Astronomy, The University of Leeds, Woodhouse Lane, Leeds LS2 9JT, United Kingdom.*

14 September 2017

## ABSTRACT

We present medium-resolution ( $R \sim 7000$ ) near-infrared echelle spectroscopic data for 36 MYSOs drawn from the Red MSX Source (RMS) survey. This is the largest sample observed at this resolution at these wavelengths of MYSOs to date. The spectra are characterized mostly by emission from hydrogen recombination lines and accretion diagnostic lines. One MYSO shows photospheric H I absorption, a comparison with spectral standards indicates that the star is an A type star with a low surface gravity, implying that the MYSOs are probably swollen, as also suggested by evolutionary calculations. An investigation of the  $\text{Br}\gamma$  line profiles shows that most are in pure emission, while  $13 \pm 5\%$  display P Cygni profiles, indicative of outflow, while less than  $8 \pm 4\%$  have inverse P Cygni profiles, indicative of infall. These values are comparable with investigations into the optically bright Herbig Be stars, but not with those of Herbig Ae and T Tauri stars, consistent with the notion that the more massive stars undergo accretion in a different fashion than lower mass objects which are undergoing magnetospheric accretion. Accretion luminosities and rates as derived from the  $\text{Br}\gamma$  line luminosities agree with results for lower mass sources, providing tentative evidence for massive star formation theories based on scaling of low-mass scenarios. We present  $\text{Br}\gamma/\text{Br}12$  line profile ratios exploiting the fact that optical depth effects can be traced as a function of Doppler shift across the lines. These show that the winds of MYSOs in this sample are nearly equally split between constant, accelerating, and decelerating velocity structures. There are no trends between the types of features we see and bolometric luminosities or near-infrared colours.

**Key words:** infrared: stars – line:profiles stars: early-type – stars:formation.

## 1 INTRODUCTION

Understanding the star formation process is of crucial importance for a number of branches of astrophysics. However, there are still gaps in our knowledge of it. Low-mass star formation is thought to result from the monolithic collapse of a cloud followed by accretion through the circumstellar disk, and is in general reasonably well understood as per the description of Shu, Adams & Lizano (1987). The mechanism through which the low mass pre-Main Sequence stars (of order few solar masses and less) further grow via this accretion disk is widely accepted to be due to magnetically controlled accretion. The infalling material flows along magnetic field lines onto the proto-star (Bertout 1989). This paradigm has been tried and observationally tested in the case of low mass T Tauri stars. A review describing much of the evidence is provided by Bouvier et al. (2007).

The theory needs to be adapted if it is to be applied to the formation of objects that are more massive. Early calculations by

Kahn (1974) showed that the radiation pressure can halt accretion for objects  $20 M_{\odot}$  and larger under spherical accretion, essentially putting an upper limit to the mass of a star. However, this mass is well below that observed from direct measurements, and theoretical efforts now converged to two main scenarios. Studies by Krumholz et al. (2009) have shown that a  $40 M_{\odot}$  star can be formed by the monolithic collapse of a dense cloud followed by disk accretion, with radiation pressure escaping along bipolar outflow cavities. A different approach has been taken by Bonnell, Bate & Zinnecker (1998) and Bonnell & Bate (2006). They propose competitive accretion as a solution to the high-mass star formation problem, whereby the most massive stars are formed at the center of dense stellar clusters. The gravitational potential of the massive star causes the gas to be funneled toward it instead of the other proto-stars, allowing it to grow quicker and to higher mass. In this scenario, a circumstellar disk is also required.

Although disk accretion seems therefore to be a main contender for the formation of massive stars, little is known about the precise accretion mechanism. Even the most recent, sophisticated star formation models are not able to simulate the fine detail re-

\* E-mail: pyrp@leeds.ac.uk

quired to probe the accretion process from parsec scales via the disk to the stellar surface. Indeed, models use a (large) volume as a sink particle in which matter falls into and assume this material will continue to form the star. For example, Rosen et al. (2016) explicitly mention that the material is not followed in the inner 80 au. Furthermore, at present, it is not at all known how the disk accretion would operate in massive stars. Once in their Main Sequence configuration, these stars are generally non-magnetic due to their radiative envelopes, their disk accretion mechanism would be different to that for the lower mass stars, where the magnetically controlled accretion operates. In this context it may be useful to note that earlier in its evolution, the star may be swollen due to the large accretion rates (Hosokawa, Yorke & Omukai 2010) and generate a magnetic field at this stage (Hoare & Franco 2007). Current evidence for pre-Main Sequence Herbig Ae/Be stars suggests the transition in disk accretion mechanism occurs around the A-B spectral type boundary (Mottram et al. 2007; Ababakr, Oudmaijer & Vink 2016). One of the few models put forward to explain the accretion mechanism in massive Herbig Be stars is the boundary layer where the circumstellar disk extends to the surface of the central star. For example, through modelling the UV spectra of a sample of Herbig Ae/Be stars, Blondel & Djie (2006) suggested these intermediate to massive stars could accrete via a boundary layer.

Next to the theoretical considerations, massive star formation poses a considerable observational challenge. High-mass protostars are rare - as predicted by the initial mass function described by Salpeter (1955) - and evolve fast, as the Kelvin-Helmholtz timescale for contraction to a main sequence (MS) configuration is shorter than the gravitational free-fall timescale. Unlike low-mass stars, they are still embedded in their parental cloud whilst accretion is ongoing. As such, they are both further away and suffer from more dust extinction than their lower mass counterparts. Therefore, observations at longer wavelengths are essential for observations of high-mass star forming regions. An important evolutionary stage for understanding the massive star formation process is the Massive Young Stellar Object phase (MYSO). These are objects which are still accreting material from their birth cloud. They are radio-weak, having not yet ionized the surrounding region to produce an HII region, in spite of their high luminosities. MYSOs are frequently associated with jets and bipolar outflows, likely driven by accretion activity. Information about the accretion process can be obtained by studying these objects, and then used to further refine theoretical models of massive star formation. Due to dust extinction, they are only visible at infrared wavelengths and longer. Overviews of the class of MYSOs can be found in Lumsden et al. (2013) and Oudmaijer & de Wit (2014).

Near-infrared (NIR) techniques can be particularly useful to study the inner 100s of au, where an accretion disk is expected to be found. Using interferometry at  $2\mu\text{m}$ , Kraus et al. (2010) directly imaged a  $\sim 15$  au scale disk around the  $20 M_{\odot}$  MYSO G310.0135+00.389, lending support to disk accretion. However, due to the limited sensitivity of current instruments, this technique can only be applied to the brightest targets, and this result has so far been the only such detection. Another approach to studying accretion disks is to look for kinematical tracers among observed NIR spectral transitions. The CO ro-vibrational lines ("bandheads") at  $2.3\mu\text{m}$  have been modelled by Chandler, Carlstrom & Scoville (1995), Wheelwright et al. (2010) and Ilee et al. (2013) to arise in warm (4000K) and dense ( $10^{10}\text{cm}^{-3}$ ) self-shielded neutral disk material in MYSOs. However, high signal-to-noise (SNR) observations at high spectral resolution are required in order to model the bandheads (as Ilee et al. 2013 note), which requires a large ob-

serving program for statistically significant conclusions about the presence of disks in MYSOs to be inferred. In addition, only a small fraction of these objects show these transitions (17 % detection rate by Cooper et al. 2013, CLO13 from here).

Stellar winds are traced by hydrogen recombination lines, particularly the Brackett series in the NIR, as modelled by Simon et al. (1981). The hydrogen recombination profiles provide clues about the line emitting region. This is possible due to the differences in the optical thickness of the various lines.

By considering the ratio of two hydrogen recombination lines, Drew, Bunn & Hoare (1993) have shown that for S106 IRS1, the hydrogen emission originates from a fast (100s km/s), optically thick wind combined with a, slower (10s km/s), optically thin nebular component. Bunn, Hoare & Drew (1995) extended this analysis to 6 more objects. They found that some objects show similar profiles to S106 IRS1, whilst others display behaviour suggestive of an accelerated stellar wind. They interpret differences in the optically thin component of the line ratio as a sign of evolutionary effects. The narrow peak will be stronger in MYSOs at later evolutionary stages, when the increasing ionizing flux generates an optically thin nebular component. Thus far, the NIR spectrum of MYSOs has been studied either in small samples at high spectral resolution, but small wavelength coverage (e.g. Ilee et al. 2013 observed a dozen objects at  $R \sim 30,000$  across CO  $2.3\mu\text{m}$ ; Blum et al. 2004 observed 4 MYSOs at  $R \sim 50,000$  across the same region; Bik, Kaper & Waters 2006 studied 20 MYSOs in the K band (between  $2.08\text{--}2.18$  and  $2.28\text{--}2.40\mu\text{m}$ ) at  $R \sim 10,000$ ;) or in large samples at broader wavelength coverage (e.g. CLO13 observed around 250 objects at  $R \sim 500$  in  $H$  and  $K$ ). In this paper we present medium resolution ( $R \sim 7000$ ) near-infrared spectra of 36 MYSOs selected from the RMS catalogue presented by Lumsden et al. (2013). This is the largest sample of MYSOs studied in this manner to date. The resolution allows studies of line profiles and detection of fainter features when compared to the lower resolution observations while the larger wavelength coverage allows for the study of a range of lines with varying excitation properties.

Section 2 describes the sample, observations, and data reduction. In Section 3 we present our assessment of dust extinction. Section 4 contains the main analysis of this paper; MYSO spectral type measurements, correlations between different line luminosities and features of the H recombination line profiles. In section 5 we present the conclusions of this research.

## 2 OBSERVATIONS

The data were obtained between 18 February and 23 July 2011 using the NIR spectrograph GNIRS on the Gemini-North telescope. 36 objects were observed over 20 nights. We used the cross-dispersed mode, coupled with the 'short' 111 l/mm camera, and a 2 pixel wide slit. Each pixel is  $0.15''$ , giving a slit width of  $0.3''$  and length of  $7''$ . The average seeing was  $0.75''$ . Since the objects are bright at  $K$ , the data were taken as a bad-weather programme, the conditions were not photometric. The observed wavelength ranges are set up in orders and centered around the positions of the  $K$ ,  $H$ ,  $J$  and  $X$  photometric bands. The  $K$  band ranges between  $2.1472$  and  $2.3355\mu\text{m}$ , the  $H$  band between  $1.6107$  and  $1.7519\mu\text{m}$ , the  $J$  band between  $1.2888$  and  $1.4017\mu\text{m}$  and the  $X$  band between  $1.0741$  and  $1.1682\mu\text{m}$ . In the following, all wavelengths for spectral lines are in vacuum. Because the sources are red, the photon count and thus the SNR is highest at longer wavelengths.

**Table 1.** Source list, including date, exposure time, position angle of the slit and known properties. 1 - Magnitudes from 2MASS; 2 - extinctions from  $H$  band continuum slope derived in this work; 3 - LSR velocities from Urquhart et al. (2011b); distances from Urquhart et al. (2011a); bolometric luminosities calculated by Mottram et al. (2011) \* - sources not in RMS database, distances and luminosities from Simon et al. (1981). \*\* - As the binarity of G110 is a new discovery and the slit was oriented E-W, we cannot accurately pinpoint the declination of the two objects. We believe the distance between them to be no more than 0.75" as given by the seeing. Luminosities, distances and LSR velocities for visual binaries given as for the whole system.

Date (2011)	RMS Name	Integration time (s)	RA (J2000)	Dec. (J2000)	PA	$m_J^1$	$m_H^1$	$m_K^1$	$A_V$ (mag) <sup>2</sup>	$V_{LSR}$ (km/s) <sup>3</sup>	Distance (kpc) <sup>4</sup>	$L_{bol}$ ( $L_\odot$ ) <sup>5</sup>	Other name
20.04	G010.8411-02.5919	960	18:19:12.1	-20:47:30.9	90	16.3	13.2	9.7	$55 \pm 3$	12.3	1.9	24000	GGD 27
29.06	G010.8856+00.1221	960	18:09:08.0	-19:27:24.0	90	15.6	12.9	9.6	$51 \pm 4$	19.7	2.7	5500	
16.05	G012.9090-00.2607	960	18:14:39.6	-17:52:02.3	60	15.3	13.2	9.2	$30 \pm 3$	36.7	2.4	32000	W33A
16.05	G014.9958-00.6732	64	18:20:19.5	-16:13:29.8	90	12.7	9.8	7.3	$39 \pm 14$	19.4	2	13000	M17SW IRS1
29.06	G015.1288-00.6717	480	18:20:34.6	-16:06:28.2	90	12.9	10.5	8.9	$25 \pm 2$	19.0	2	12000	
29.05	G017.6380+00.1566	64	18:22:26.4	-13:30:12.0	90	15.0	12.7	7.3	$93 \pm 3$	22.1	2.2	100000	AFGL 2136
18.06	G018.3412+01.7681	960	18:17:58.1	-12:07:24.8	0	15.3	12.9	9.3	$53 \pm 7$	33.1	2.8	22000	
9.07	G023.3891+00.1851	304	18:33:14.3	-08:23:57.4	90	15.8	11.6	8.4	$47 \pm 3$	75.5	4.5	24000	
16.07	G025.4118+00.1052_A	480	18:37:16.9	-06:38:29.8	90	17.2	15.7	12.9	$61 \pm 1$	95.3	5.2	9700	
23.07	G026.2020+00.2262	456	18:38:18.5	-05:52:57.4	90	14.2	10.6	8.3	$37 \pm 4$	112.4	7.5	3600	
20.07	G026.3819+01.4057_A	480	18:34:25.7	-05:10:50.2	90	13.1	10.8	9.1	$33 \pm 6$	42.1	2.9	17000	
22.07	G027.7571+00.0500	960	18:41:48.0	-04:34:52.9	90	16.7	13.0	9.3	$59 \pm 16$	99.6	5.4	13000	
29.06	G029.8620-00.0444	960	18:45:59.6	-02:45:06.5	50	15.1	12.5	9.8	$43 \pm 5$	101.2	4.9	28000	
20.05	G030.1981-00.1691	960	18:47:03.1	-02:30:36.1	90	17.0	12.6	9.3	$53 \pm 4$	103.1	4.9	30000	
20.05	G033.3891+00.1989	64	18:51:33.8	+00:29:51.0	90	13.0	9.6	7.2	$33 \pm 4$	85.3	5	13000	GGD 30 IRS 3
20.07	G033.5237+00.0198	960	18:52:26.7	+00:32:08.9	90	15.8	12.0	8.9	$45 \pm 4$	103.5	7	13000	
22.07	G034.0500-00.2977_A	304	18:54:31.9	+00:51:32.6	90	14.1	12.2	11.0	$11 \pm 3$	11.5	12.9	23000	
22.07	G034.0500-00.2977_B	304	18:54:32.3	+00:51:33.2	90	11.0	9.6	8.4	$21 \pm 4$				
23.07	G034.7123-00.5946	960	18:56:48.3	+01:18:47.1	90	18.4	13.4	9.2	$59 \pm 4$	44.5	2.9	9700	
22.04	G056.4120-00.0277	160	19:36:21.5	+20:45:17.9	90	12.5	9.9	8.1	$31 \pm 2$	-4.4	9.3	22000	
10.06	G073.6525+00.1944	960	20:16:22.0	+35:36:06.2	55	13.9	11.5	9.6	$31 \pm 7$	-73.4	11.2	100000	
25.06	G073.6952-00.9996	120	20:21:18.9	+34:57:50.9	0	12.9	10.6	8.0	$47 \pm 5$	-31.3	7.4	17000	
16.07	G076.3829-00.6210	24	20:27:26.8	+37:22:47.7	90	10.4	7.7	5.9	$31 \pm 5$	-1.7	1.4	40000	S106 IRS1
10.06	G077.4622+01.7600_A	480	20:20:39.3	+39:37:58.5	150	12.8	10.6	8.9	$39 \pm 4$	2.1	1.4	3100	
24.06	G078.8867+00.7087	40	20:29:24.0	+40:11:19.4	0	14.3	10.8	6.6	$65 \pm 2$	-6	3.3	200000	AFGL 2591
23.06	G094.3228-00.1671	960	21:31:45.1	+51:15:35.3	90	15.4	12.0	9.8	$47 \pm 18$	-38.4	4.4	5700	CPM 15
16.07	G094.6028-01.7966	48	21:39:58.3	+50:14:20.9	90	10.9	9.2	6.8	$29 \pm 3$	-43.9	4.9	43000	V645 Cygni
21.07	G102.3533+03.6360	48	21:57:25.2	+59:21:56.6	90	12.3	9.6	7.2	$39 \pm 2$	-88.6	8.4	110000	CPM 36
22.07	G106.7968+05.3121*	24	22:19:18.2	+63:18:47.0	64		8.1	6.1	$59 \pm 1$		0.9	13000	S140 IRS1
21.07	G110.1082+00.0473B_A	480	23:05:10.2	+60:14:42.7**	90	10.7	10.0	10.1	$3 \pm 3$	-52.1	4.3	17000	
21.07	G110.1082+00.0473B_B	480	23:05:10.3	+60:14:42.7**	90		9.8	9.5	$3 \pm 1$				
26.06	G111.2348-01.2385	960	23:17:21.0	+59:28:48.0	10	14.1	11.3	9.6	$73 \pm 3$	-54.4	4.4	42000	IRAS 23151+5912
21.07	G111.5234+00.8004A	96	23:13:32.4	+61:29:06.2	45	11.1	9.7	7.8	$35 \pm 3$	-58.6	2.6	5600	NGC 7538 IRS 4
25.06	G111.5423+00.7776	200	23:13:45.4	+61:28:10.3	80	14.6	11.6	8.5	$91 \pm 3$	-57.2	2.6	210000	
21.07	G120.1483+03.3745	48	00:23:57.0	+66:05:51.5	90	11.8	9.0	7.0	$33 \pm 4$	-68.9	5.6	21000	CPM 1
18.02	G151.6120-00.4575	48	04:10:11.9	+50:59:54.4	90	10.9	8.9	7.1	$27 \pm 3$	-49.7	6.4	61000	CPM 12
18.02	G213.7040-12.5971_A*	80	06:07:47.8	-06:22:56.2	14	13.1	11.4	7.2	$31 \pm 2$		0.95	25000	Mon R2 IRS3A
18.02	G213.7040-12.5971_B*	80	06:07:47.9	-06:22:55.4	14		9.5	7.3	$31 \pm 2$				Mon R2 IRS3B
18.02	G233.8306-00.1803	24	07:30:16.7	-18:35:49.1	60	10.9	8.0	6.1	$35 \pm 14$	44.6	3.3	13000	

The observed sources were selected from the RMS database (Lumsden et al. 2013). Two objects (G106.7968 and G213.7040) are not in the RMS database as they are located at a high galactic latitude. For these, the distance and bolometric luminosity are taken from Simon et al. (1981). The selection criteria included a source classification as MYSO, observability from Gemini-N, and being bright enough at  $K$  to result in good SNR spectra at these wavelengths. Emphasis was put on obtaining data from the most luminous objects fulfilling those criteria. 90% of the observed objects are bright ( $L > 8000 L_{\odot}$ ) and radio-quiet, and all have  $L > 3000 L_{\odot}$  and radio flux  $< 0.5$  Jy at 5 GHz. As such, they likely have not yet started to ionize the ISM and produce an HII region. The sample properties are described in the Table 1.

Most targets are compact enough to allow nodding along the slit in an ABBA sequence to remove the sky background. For extended sources a sky region outside of the nebula was used. Spectra of nearby main sequence stars of types B9V-A4V were obtained in order to correct for atmospheric telluric absorption. The airmass difference between these and the science targets was always less than 0.1. Stars with these spectral types were used as they have few intrinsic absorption features in the wavelengths of interest to this work. Where necessary, their absorption features were fitted and removed prior to telluric line correction. A standard reduction procedure was applied to all the spectra, using the *PyRAF* package (Science Software Branch at STScI 2012). The bias and dark subtraction are done in the pre-reduction phase at the telescope. Pixel-to-pixel variations were corrected for by using flat-field frames. The sky background was removed with the standard ABBA subtraction. One-dimensional spectra from each order were then extracted. Argon lamp spectra and telluric absorption lines from the solar spectrum of Hinkle, Wallace & Livingston (1995) were used to perform the wavelength calibration. The resulting calibration was assessed by measuring the wavelengths of telluric lines. The wavelength calibration was found to be accurate to  $\sim 5$  km s $^{-1}$ . The resolution of the spectra as measured from the arc calibration lines is in the range 35-49 km s $^{-1}$ , corresponding to  $R \approx 7000$ . The  $K$  and  $H$  band spectra have high SNR ( $> 100$  for most spectra), while 66% of the  $J$  and 50% of the  $X$  bands have SNR  $> 30$ .

The intrinsic absorption features of the telluric standards were removed by using Voigt profiles. This proved particularly difficult for the Br10 line at  $1.737 \mu\text{m}$ , as a number of telluric lines are blended with this HI line. As such this recombination line was not used in our analysis. The calibrated target spectra were then divided by the telluric standard (with the intrinsic features removed), in order to remove the atmospheric absorption features. The result is multiplied by a blackbody of the temperature of the telluric standard star to retrieve the relative photometric shape of the target spectra. The spectra were not obtained in photometric conditions, as accurate flux calibration was not the main aim of the observations. However, when using differential count ratios between the different bands in spectra of individual objects, the resulting colour agreed to within 0.5 magnitude with those from 2MASS.

The fact that relative count rates return fairly good estimates of the colours, allowed us to determine the continuum fluxes of MYSOs in the  $X$  band ( $1.09 \mu\text{m}$ ). The scaling factor was derived by using the relative count rates between  $X$ ,  $J$ ,  $H$ , and  $K$ , with the respective colours of the telluric standard stars (whose continuum flux at  $1.09 \mu\text{m}$  were obtained by interpolating between their fluxes at the  $J$  and  $I$  photometric bands). The MYSO spectra were then scaled at the given 2MASS central band wavelengths.

For the computation of line fluxes, we use catalogued photometry from 2MASS (Skrutskie et al. 2006). We also considered

UKIDSS (Lucas et al. 2008), but find that using the UKIDSS photometry results in an discontinuous spectrum between different orders for a large fraction of our sample. The reason for this is the sensitivity of the UKIDSS survey. Many of the targets have  $m_K < 10$ , which often leads to saturation in UKIDSS. Where 2MASS data was not available, the MYSO magnitudes were estimated from the telluric star magnitude, with as caveat that the fluxes carry large errorbars - 0.4 magnitudes in the  $K$  band.

The velocity from the Br $\gamma$  line was compared to values from the RMS database, as reported by Urquhart et al. (2011b). The deduced LSR velocities agree very well with the RMS LSR velocities from NH $_3$  surveys, with a Pearson correlation factor of 0.89, and a scatter of 6.5 km/s around the best fitting line. The other recombination lines yielded similar results, implying that the objects are associated with the high density clouds probed by RMS.

### 3 EXTINCTION

The determination of the dust extinction to the target objects, and the subsequent correction for it, are problematic in the case of MYSOs. As explained in the introduction, these regions are considerably affected by dust. In the sample of CLO13 of 135 MYSOs, the extinctions found ranged between  $2.7 < A_V < 11.4$ .

We estimate the extinction using the slope of the continuum, in a similar manner to Porter, Drew & Lumsden (1998). The spectra of MYSOs show a rising red continuum, which is caused by a combination of reddening of the stellar photosphere by dust extinction on the one hand and thermal emission by dust on the other hand. Martin & Whittet (1990) derive that  $A_{\lambda} \propto \lambda^{-1.8}$  between  $1-4 \mu\text{m}$  (see also Moore et al. 2005 for the case of high  $A_V$ ). The Rayleigh-Jeans (RJ) approximation can be used for a blackbody at NIR wavelengths, i.e.  $F_{\lambda} \propto \lambda^{-4}$ . We determine the value of the extinction that produces a dereddened spectrum with a slope closest to that of the RJ approximation through chi-squared minimisation. We compute values for  $A_V$  for each of the spectral bands of an object in this manner. The errors are determined from the chi-squared analysis. The  $K$  band yields the highest value for  $A_V$ , this is most likely due to dust emission starting to contribute significantly at these wavelengths. Porter, Drew & Lumsden (1998) demonstrated that extinctions derived from the continuum slope at the shorter  $J$ ,  $H$  bands are in agreement with those from the line fluxes of the hydrogen lines assuming case B recombination<sup>1</sup>. Most of our sources are too embedded to be detected in the  $J$  or  $X$  bands, or have too low an SNR for extinction estimations from the continuum slope. We therefore choose to use the extinction obtained from the spectral slope of the  $H$  band continuum in all of the following analysis, as the effect of hot dust excess is considerably lower than in the  $K$  band. The values are listed in Table 1.

### 4 RESULTS

We begin this section with an overview of the spectra and their characteristics. We then discuss the absorption lines focussing on the hydrogen lines that are found in absorption towards 2 objects, allowing their spectral types to be derived. This is followed by an analysis of the emission lines, their fluxes and their profiles, while

<sup>1</sup> Their observed hydrogen recombination lines covered a larger wavelength range than ours, which prevents us from making a similar estimate.

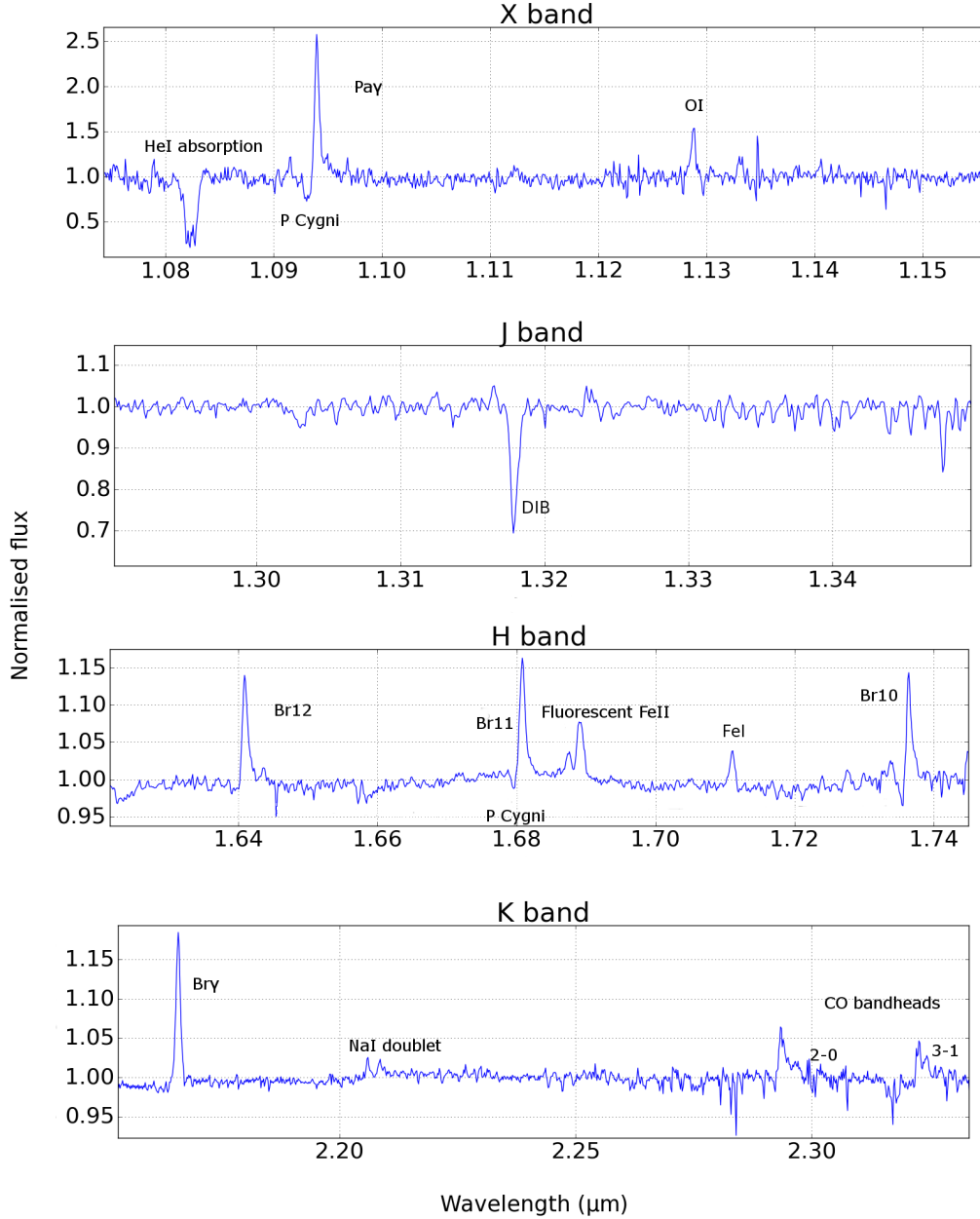


**Figure 1.** Example spectrum of G056.4120-00.0277, continuum normalized. From bottom to top, the data correspond to the *K*, *H*, *J* and *X* bands respectively.

hydrogen emission line profile ratios are used to learn about the line formation regions.

#### 4.1 Description of spectra

An example spectrum, of G056.4120-00.0277, is presented in Figure 1. The HeI transition at  $1.083\mu\text{m}$ , as well as the  $\text{Pa}\gamma$  hydrogen recombination line at  $1.094\mu\text{m}$  are present in the X-band. Strong telluric absorption hinders the detection of spectral lines in the red part of this band. Strong telluric absorption minimizes the use of the *J* band past  $\sim 1.35\mu\text{m}$ . The only transitions in the observable range are the OI line at  $1.316\mu\text{m}$ , which is seen towards some sources, as well as strong Diffuse Interstellar Band (DIB) absorp-

tion at  $1.318\mu\text{m}$ . The *H* band spectrum is marked by three strong Brackett series transitions - 12-4 at  $1.641\mu\text{m}$ , 11-4 at  $1.681\mu\text{m}$  and 10-4 at  $1.737\mu\text{m}$ . A number of Fe transitions are also present, such as the shocked [FeII] transition at  $1.644\mu\text{m}$ , the fluorescent FeII transition at  $1.689\mu\text{m}$ , as well as another FeI line at  $1.711\mu\text{m}$ . The strongest feature in the *K* band is the  $\text{Br}\gamma$  line at  $2.166\mu\text{m}$ . Other transitions observed in the *K* band are the NaI doublet at  $2.206$  and  $2.209\mu\text{m}$ , and the shocked  $\text{H}_2$  transition at  $2.24\mu\text{m}$ . Finally, the first two CO first-overtone bandhead transitions, located at  $2.29$  and  $2.32\mu\text{m}$  are also covered.

The detection rates of various lines are presented in Table 2. Virtually all objects have  $\text{Br}\gamma$  in emission. The detection rate of the higher Brackett lines is slightly smaller, which can be attributed to

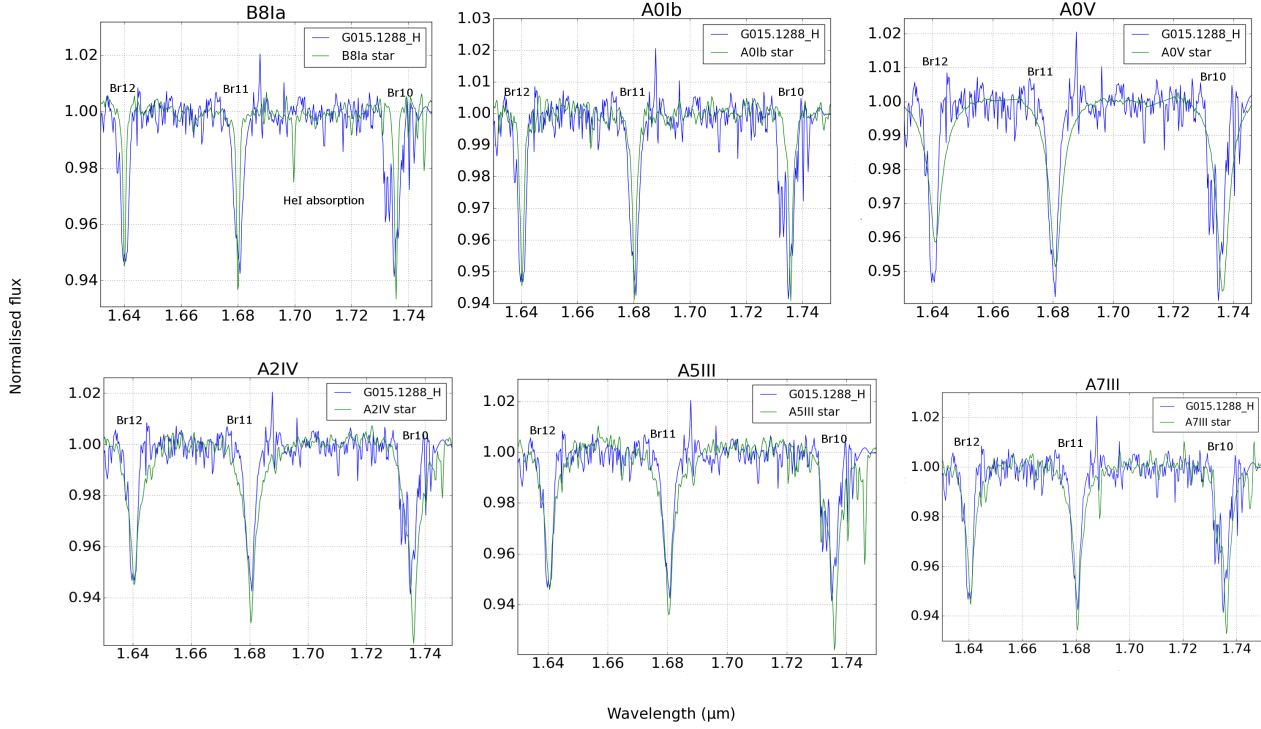


**Figure 2.** Br10-12 profiles in G015.1288-00.6717 (blue) compared with normal stars with added continuum dust excess (green). Data from Meyer et al. (1998) and Hanson et al. (2005). See text for details.

**Table 2.** Detection rates of various features observed in our sample, compared to their respective values in the CLO13 survey. A number of lines that we find were not detected in the previous survey. The higher spectral resolution allows for fainter lines to be detected, while the current *H* wavelength coverage is broader than in CLO13.

Spectral line	Br $\gamma$	Br12	Br11	Br10	Pa $\gamma$	H2	NaI	CO emission	[FeII]	fluorescent FeII	OI	HeI
Detection rate	97%	82%	79%	79%	26%	21%	37%	34%	42%	61%	21%	24%
CLO13 rate	75%	44%	37%	45%	N/A	9%	N/A	17%	34%	26%	N/A	N/A

the fact that these lines are intrinsically weaker, and therefore less prone to detection. Overall, the detection rates are much higher than in CLO13, which can be readily explained by the superior spectral resolution employed here, facilitating the detection of weaker lines that were unresolved by CLO13.

Three objects (G034.0500-00.2977, G110.1082+00.0473B and G213.7040-12.5971) showed two separate spectra within the slit, which, when extracted, appear to be objects with different spectra, and which thus may form a binary system. G034.0500 is referred to in the RMS database as a binary source, whereas the binarity of G213.7040 and G110.1082 are new findings. However, in the absence of other data to confirm binarity we stress that it is possible these are visual binaries rather than bound systems.

## 4.2 Absorption lines

### 4.2.1 Spectral typing

The stellar parameters can not be determined in the usual manner as the targets are invisible at blue wavelengths - the classical wavelength regime for spectral typing. At near-infrared wavelengths the MYSO photospheres are heavily veiled by dust emission, and spec-

tral typing is difficult as well. In practice, spectral types of MYSOs are usually estimated using the total luminosity derived from Spectral Energy Distribution (SED) fitting.

Traditionally, MYSOs have been found to have luminosities similar to those of OB stars. Spectral types have rarely been determined directly in MYSOs, and not at all in the case of RMS MYSOs. Previously, Kendall, de Wit & Yun (2003) observed *H*-band spectra of three MYSOs, IRAS 17175-3544, 17441-2910 and 18079-1756 at intermediate resolution ( $R \sim 5000$ ). They found photospheric absorption lines in IRAS 18079-1756 and IRAS 17175-3544, and assigned spectral types of B3V and O7-8V respectively to these two objects.

Most of our MYSOs show strong, broad HI emission, due to a stellar wind (see also Sec. 4.3). However, two of the objects in this sample (G015.1288-00.6717 and G034.0500-00.2977\_A) display absorption in the Br10, Br11 and Br12 lines. There are also hints of absorption in Br $\gamma$  and Pa $\gamma$ , alongside the dominant emission in these two objects. The RMS survey quotes G015.1288 as having  $L_{\text{bol}} = 13000 L_{\odot}$ . This corresponds to a spectral type of B0.5 for a Zero-Age Main-Sequence star, using the values from Straizys & Kuriliene (1981).

The absorption profiles in the *H* band of G015.1288 were

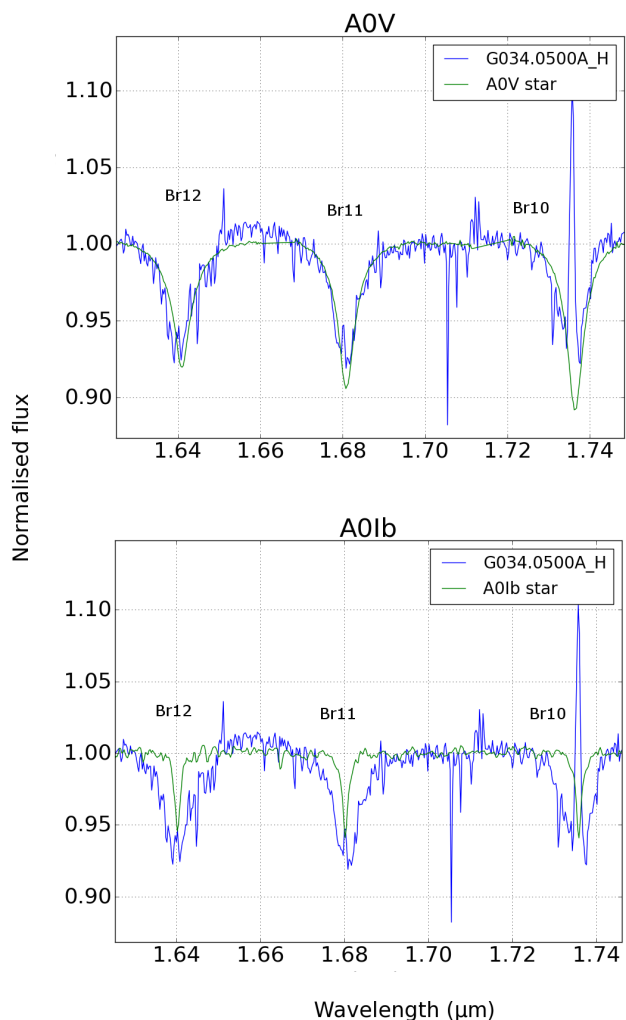


**Figure 3.** Spectral typing of G034.0500-A. The Brackett absorption lines are too large compared to what would be expected of a A0Ib star, they are more like an A0V.

compared with spectra of normal stars from the surveys of Hanson et al. (2005) and Meyer et al. (1998). A spectral type of F or later would be hard to reconcile with the MYSO data, as F stars have a large number of metal lines. In addition, early O spectral types do not match either, as their Brackett lines are weaker and narrower than observed for G015. Late O and B1-5 stars show a HeI line at  $1.70 \mu\text{m}$ , at comparable or higher strength than the hydrogen absorption lines, and is not present here. We note that the near-infrared spectral surveys of Hanson et al. (2005) and Meyer et al. (1998) do not have complete spectral and luminosity type coverage. The only B type sample spectra available are those for B1, B5 and B8.

So, given the presence and absence of diagnostic absorption lines, a spectral type later than B5 and earlier than A9 would be expected for G015.1288. However, the Br10-12 absorption in the B5-A9 stars is much stronger than observed for G015.1288. It is possible that a significant amount of excess could veil the HI absorption to a comparable level to our observations. This is illustrated in Figure 2, which zooms in on the Brackett lines in the  $H$  band spectra of a number of normal B8-A7 stars with added excess continuum emission. Overplotted on these are the GNIRS data

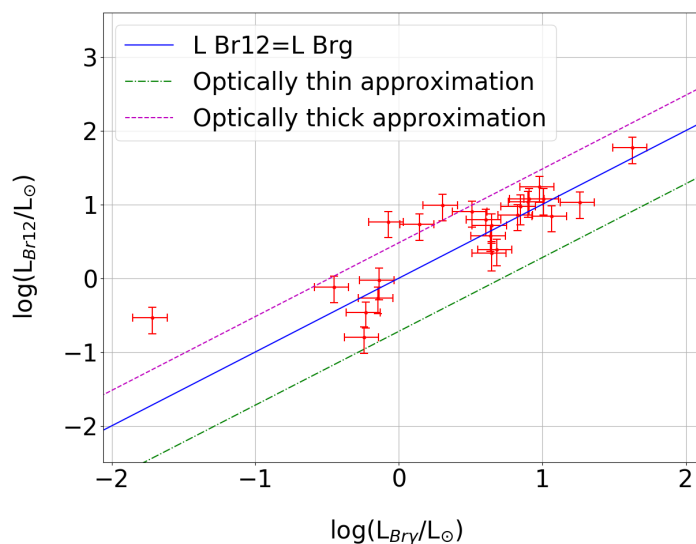


**Figure 4.** Br12 luminosity as a function of  $\text{Br}\gamma$ , with optically thin and optically thick approximations, and a equal luminosity line.

for G015.1288. A B8 star with added excess does not match the observed HI profiles, as the lines in this star are considerably narrower than in G015.1288. In addition, the HeI line is still strong enough to be observed. The A0Ib profiles match the observations in strength, but are narrower. An A0V star has broader wings in the Brackett lines than G015.1288. In the absence of more observational Main Sequence star spectra to compare our data with, we conclude that G015.1288 has the spectrum of an early A giant or supergiant, with an excess continuum added to the stellar photosphere corresponding to  $4\times$  the continuum at  $H$ .

We applied a similar analysis to the Br10-12 absorption lines in the spectrum of G034.0500-00.2977\_A. In this case the lines are considerably broader, and we find the best fit is that of an A0V (MS-like) star, as can be seen in Figure 3. In contrast, the spectrum of G034.0500-B shows the usual NIR rising red continuum of MYSOs.

A full study of the binary system is beyond the scope of this paper. However, given that a lower mass object will be in an earlier evolutionary stage than a higher mass object of the same age, it is more likely that G034.0500-00.2977\_A is a main sequence star located in the same direction as source B, rather than a lower mass star-forming object associated with a MYSO.

In summary, the (only) observed absorption spectrum of a MYSO in the present sample can be reproduced by an A-type object with a relatively low surface gravity. We need to invoke a continuum excess emission of a factor of a few in order to match the lower depth of the lines. This excess is due to radiation from hot dust, and does not affect the spectral classification itself, as that is based on the linewidths and relative strengths of absorption lines, both of which do not change after the addition of a continuum excess. For a typical temperature of 10,000 K of an A0 star and an observed luminosity of  $13,000 L_{\odot}$ , we infer a stellar radius of order  $70 R_{\odot}$  for G015.1288.

The fact that the star is cooler and larger than what we might expect based on its total luminosity can be understood in terms of the high accretion expected in massive star forming objects. Constant accretion simulations done by Hosokawa, Yorke & Omukai (2010), as well as more recent hydrodynamic simulations done by

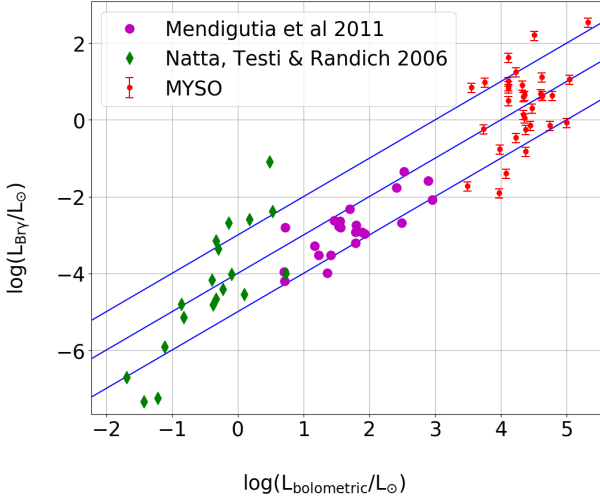


**Figure 5.** Log-log plot of the luminosity in the Br $\gamma$  line against bolometric luminosity. Green diamonds are T Tauri stars, while purple circles are Herbig stars, objects of a lower and intermediate mass, respectively, believed to be at a similar evolutionary stage as MYSOs. The solid lines correspond to  $\dot{L}_{Br\gamma} = 10^{-3} L_{bol}$ ,  $10^{-4} L_{bol}$  and  $10^{-5} L_{bol}$

Haemmerlé & Peters (2016) show that a pre-MS star accreting at a constant rate of  $10^{-3} M_{\odot} \text{yr}^{-1}$  can swell up to 40-300  $R_{\odot}$ . With constant luminosity, this puffing up will cause a decrease in temperature of a factor  $\sim 3$ . A puffed up late-O/early-B type star will have a temperature and structure similar to an A-type giant or supergiant star. This might explain why MYSOs have yet to ionize their surroundings and form an HII region, as the UV flux of an A star is considerably lower than that of a B star (cf. Hoare & Franco 2007).

#### 4.2.2 Other absorption lines

Turning to other absorption lines, as can be seen in Figure 1, the strongest absorption feature in the spectrum is located at  $1.318 \mu\text{m}$ . We identify this absorption with the  $\lambda 13175$  (Å) Diffuse Interstellar Band (Cox et al. 2014; Hamano et al. 2015). It is detected in most objects for which useable  $J$ -band data were obtained, and the equivalent widths are measured to be up to several Å. The lines in the MYSOs are much stronger than reported thus far in the literature and this can be partly understood due the fact that the extinction towards the targets is much larger than those for example sampled in Cox et al. (2014) and Hamano et al. (2015), whose highest extinction lines of sight have an  $A_V$  of 10. These authors also determine the slope of the relationship between the DIB's EW and  $A_V$ . The EWs of the band in the MYSOs do not follow these relationships however; the lines are weaker than the  $A_V$  values would imply. In understanding this finding, we need to consider that the total extinction towards our targets is a combination of foreground (interstellar) extinction and extinction due to the dust in the parental molecular cloud and circumstellar envelopes. It had been observed previously that the DIBs do not trace circumstellar material as efficiently as they trace the interstellar material. This could be due to different excitation conditions in these respective environments, the net effect is that the line-EWs are indeed lower than the total  $A_V$  would suggest (Oudmaijer, Busfield & Drew 1997).

Finally, we also observe CO bandhead absorption lines, which

is expected to originate from a further out, colder component than its emission counterpart (Davies et al. 2010). Studies of these lines can help in determining the properties of the outer, cooler envelope of MYSOs, but their analysis is beyond the scope of this study.

### 4.3 Emission lines

We have compiled an atlas of the spectral features found in the data (presented in the Appendix). We consider a spectral line a detection if it has a peak flux  $F_{\lambda} > 3\delta F_{cont}$ , and a full-width half-maximum larger than the resolution limit where  $\delta F_{cont}$  is given by the root-mean-square variations of the continuum counts. The continuum normalised lines were fitted with Gaussian profiles.

#### 4.3.1 Line luminosities and accretion rates

Let us first discuss the line luminosities which are computed using the distances and the measured Equivalent Width and the dereddened continuum fluxes.

The lines in the Brackett series form in similar conditions. For example, in the case B approximation, the ratio  $Br\gamma/Br12 \simeq 5 \pm 1$ , for temperatures between 3000-30000K and electron densities  $10^4$ - $10^9 \text{ cm}^{-3}$ . In the optically thick case, the Rayleigh-Jeans approximation applies and the ratio is given by  $Br\gamma/Br12 = (\lambda_{Br12}/\lambda_{Br\gamma})^{-4} S_{Br\gamma}/S_{Br12}$ , where  $S$  is the projected surface area the line is emitted from. If both lines are emitted from an area of the same size, the ratio becomes 0.33, the lower limit. The Br12 and Br $\gamma$  luminosities indeed correlate, as shown in Figure 4. Most points lie between the optically thin and optically thick approximations. The optical thickness of these regions depends on the type of wind present, which we will return to in Section 4.3.5. CLO13 found that Br $\gamma$  luminosities lie between  $\log(L_{Br\gamma}) = \log(L_{bol}) - 3$  and  $\log(L_{bol}) - 5$ . This result is confirmed by the GNIRS data, as can be seen in Figure 5. We also plot data of intermediate mass pre-Main Sequence Herbig Ae/Be stars from Mendigutía et al. (2011) and low mass T Tauri stars from Natta, Testi & Randich (2006) for comparison with lower mass sources. These seem to also lie within the same ranges as our data, indicating that there is some degree of continuity across the mass range of different pre-Main Sequence objects.

The luminosity of the Br $\gamma$  line, and many other emission lines, has been shown to be a proxy for the accretion luminosity in low and intermediate-mass YSOs (Mendigutía et al. 2011; Natta, Testi & Randich 2006). It stems from the observed correlation between the Br $\gamma$  line luminosity with the accretion luminosity - which is essentially the kinetic energy of the infalling material converted into radiation in the accretion shock. The hydrogen recombination line emission is seen to originate in the accretion funnels in the lower mass T Tauri stars, whereas it appears to trace winds in the higher mass Herbig Be stars (see e.g. Fairlamb et al. 2015). The reasons for the apparent contradiction that the line luminosity - accretion luminosity correlations hold in both situations can be intuitively explained by the fact that the hydrogen is ionized by the radiation emerging from the accretion shock region, leading to a relationship between accretion and hydrogen recombination emission. In principle, therefore, we can exploit the correlation and proceed with computing accretion luminosities from the Br $\gamma$  lines.

Following CLO13, we calculate accretion luminosities from Br $\gamma$ . To this end we use the Mendigutía et al. (2011) relation:

$$\log(L_{acc}/L_{\odot}) = (3.55 \pm 0.80) + (0.91 \pm 0.27) \log(L_{Br\gamma}/L_{\odot}) \quad (1)$$

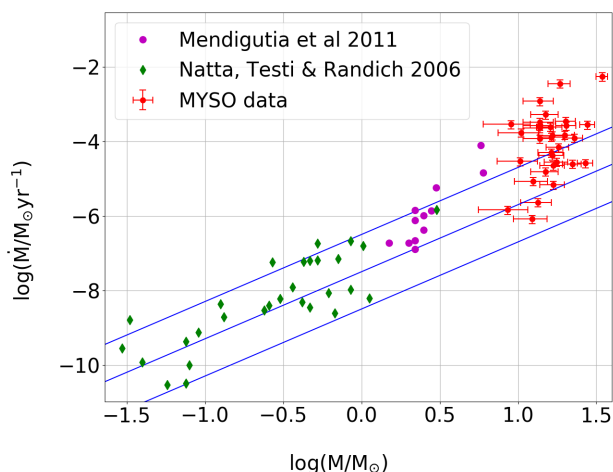


**Figure 6.** Log-log plot of the mass accretion rate against stellar mass. The symbols are as the previous figure. The solid lines correspond to  $\dot{M}=10^{-5.5} M_*$ ,  $10^{-6.5} M_*$  and  $10^{-7.5} M_*$ .

This results in accretion luminosities of MYSOs in the range  $L_{acc} = 0.1-10 L_{bol}$ . From the accretion luminosity we can determine the mass accretion rate if we know the mass and radius of the star, with the following formula:

$$\dot{M}_{acc} = \frac{L_{acc} R_*}{GM_*} \quad (2)$$

Masses and radii are estimated from the bolometric luminosities using the Zero Age Main Sequence relations as tabulated by Davies et al. (2011), ( $M \propto L_{bol}^{0.33}$ ,  $R \propto L_{bol}^{0.2}$ ). Figure 6 shows the resulting accretion rates against stellar mass. The mass accretion rates lie above  $\log(\dot{M}_{acc}) = -6.5 + 1.8 \log(M_*)$ , similarly to lower mass objects, but also extend to above the  $\log(\dot{M}_{acc}) = -8.5 + 1.8 \log(M_*)$  line, unlike the low mass sources. It would appear that the results for the MYSOs follow the trend of increasing mass accretion rate with mass as observed for the lower mass T Tauri and Herbig Ae/Be stars, a trend that was also pointed out by Beltrán & de Wit (2016) and CLO13. However, the MYSOs' mass - mass accretion rate relation can be a fit by  $\log(\dot{M}_{acc}) = (-7.0 \pm 1.4) + (2.4 \pm 1.2) \log(M_*)$ , which is a steeper line than  $\log(\dot{M}_{acc}) = -7.5 + 1.8 \log(M_*)$ , which was the best fit for the low-mass T Tauri stars. It is possible that MYSOs have A supergiant configurations, from the results in Section 4.2.2. As the stars are larger and hence the gravitational potential being released per unit mass will be smaller, including this effect will thus result in accretion rates that will be about an order of magnitude higher.

#### 4.3.2 Other line luminosities

Not only the Br12 and Br $\gamma$  line luminosities correlate (Figure 4), 75% of the lines' luminosities studied here correlate with one another with a probability of false correlation of under 1%. As example, we find that CO bandhead, when in emission, and Br $\gamma$  luminosities strongly correlate (see Figure 7, in agreement with the results of Ilee et al. 2014). We find a best fit line to detections of  $\log(L_{CO}) = (0.49 \pm 0.11) + (0.80 \pm 0.09) \log(L_{Br\gamma})$ , and when including upper limits, this becomes  $\log(L_{CO}) = (-0.95 \pm 0.12) + (0.85 \pm 0.11) \log(L_{Br\gamma})$ .

There are two issues that we need to highlight here. Firstly, the CO bandhead emission arises from the warm, dense circumstellar

**Table 3.** Fraction of objects with different type of profile features. Objects can display more than one feature.

	Br $\gamma$ /Br12
Flat	19%
Wide peak	26%
Narrow peak	26%
Dish	19%
Dish + peak	11%
Central dip	15%
Red asymmetry	15%
Blue asymmetry	15%

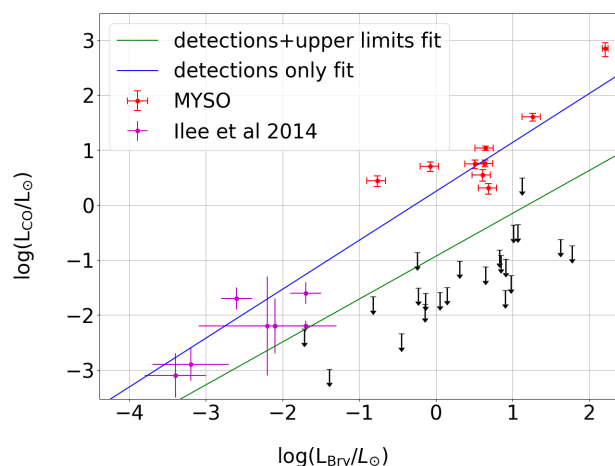


**Figure 7.** Log-log plot of the CO bandhead luminosity as a function of Br $\gamma$  luminosity, with data from GNIRS and Ilee et al. (2014)

disk material which is not necessarily directly associated with the ionized wind or present-day accretion flows. It is thus interesting that the luminosity of emission lines originating from these very different regions are correlated. A logical further step is that the correlation itself will also allow one to derive the mass accretion rates from the CO bandhead emission, despite the fact that the line forming region does not need to have a direct relationship to the accretion process. Secondly, the correlation is very strong when the CO bandhead is in emission, but a large fraction of the stars in the sample does not have (detected) emission. The upper limits to the line luminosities for the non-detections lie in some cases several orders of magnitude below those of the detections, which prompts the question why the detections themselves would correlate with the Br $\gamma$  line luminosities at all.

A first conclusion of this would be that there may be an underlying relation between these lines causing their luminosity to correlate. In the case of the Br $\gamma$  line, which is more likely to be formed in a wind rather than in an accretion funnel (see the discussion later on line profiles), it could be argued that accretion and outflows are intimately linked as winds can be accretion powered and thus correlated with the accretion rates. However, many lines arise from different regions and it will be hard to apply this explanation to all lines. Indeed, in a recent study on Herbig Ae/Be and T Tauri stars, Mendigutía et al. (2015) have shown that the origin of line correlations with accretion luminosities are caused by both of these quantities being correlated with stellar luminosity. This may well

be the case for MYSOs too, with correlations seen being a scaling effect as the emission line strengths are proportional to the stellar luminosity. Hence brighter, more massive, stars will have stronger emission lines, as well as a stronger continuum flux.

#### 4.3.3 HII region contributions to recombination lines

In the previous sections we attributed all of the Br $\gamma$  line luminosity to accretion. However, this assumes that there is no contribution from low density ionised gas like that of an HII region. Here we assess the plausibility of this assumption by analysing the possible presence of an HII region in the sample objects.

Firstly, one would expect a much stronger Br $\gamma$  line (4–5 $\times$  continuum level) than what we observe in our survey, where the average Br $\gamma$  strength is 1.3 $\times$  continuum. Recombination lines in HII regions are also narrower compared to our sample average of 150 km/s (typical FWHM of 30–40 km/s e.g. Lumsden & Hoare 1996, Burton et al. 2004).

In addition, another means of revealing the presence of an HII region is by detecting strong free-free emission at 5 or 9 GHz. Most of our sources are undetected at these radio frequencies at the 5 mJy level (Urquhart et al. 2009, or in subsequent RMS database observations).

Several of our sources have been observed at high-resolution in the sensitive radio observations of Rosero et al. (2016). Their morphologies show little evidence of an HII region structure. Instead, the radio continuum is dominated by jet emission. Following Purser et al. (2016) we produce a plot of radio flux as a function of bolometric luminosity in Figure 9 and we compare the MYSOs with expected values for HII regions from Davies et al. (2011) and jets from Anglada (1995). We find that given their bolometric luminosity almost all of our sources are too faint in the radio to be an HII region. Four objects are detected at 9 GHz (G110.1082B, G076.3829, G111.5423 and G010.8411), with only G110.1082B being close to the HII region line. However, this MYSO is located 5'' away from an HII region (G110.1082A), and the radio flux is integrated over both A and B sources.

Given the above, we conclude that the contribution of HII region emission to the total Br $\gamma$  flux is minimal.

#### 4.3.4 Profile shapes

One of the main advantages of this data set is the spectral resolution. This allows for an analysis of the line profiles. Following the prescriptions of Cauley & Johns-Krull (2015), who performed an analysis of line profiles in Herbig Ae/Be stars, we divide the profile features into 6 different categories: E - single-peaked emission, A - absorption, PC - P Cygni profile, IPC - inverse P Cygni profile, D - double peaked profile and N - non-detection. The results are presented graphically, for the main observed lines, in Figure 8.

For most lines, single-peaked emission is the most frequent feature type. The relative fractions of single peaked emission fractions to other feature types are similar for all HI recombination lines. Blueshifted P Cygni-type (PC) absorption, indicative of outflowing material, is fairly rare; it is seen in all HI lines in three MYSOs, in Br10–12 in two other objects, and in HeI in 4 objects. Redshifted inverse P Cygni-like (IPC) absorption, indicative of infall, is seen in three objects in Br $\gamma$  and one in HeI. The occurrences of P Cygni and inverse P Cygni lines are 13% and 8% respectively. These are lower than the values found by Cauley & Johns-Krull (2015) for Herbig Ae/Be stars, which in turn were found to be lower than those

for T Tauri stars. They also found that more Herbig Ae than Herbig Be stars show IPC lines, which they take as indication of the differences between the dominant accretion processes involved in these objects.

Our fractions of PC and IPC profiles show that this trend continues to higher mass MYSOs. The PC velocities extend as far as 600–800 km/s, and IPC up to 200–300 km/s.

An example of the Br $\gamma$  profiles can be seen in Figure 10.

#### 4.3.5 Hydrogen line profile ratios

As shown in Section 4.3.4, many observed HI recombination line profiles show asymmetries, suggesting that there are multiple components giving rise to the observed emission. In order to disentangle these, we analyse the recombination line ratios. These can provide clues on the formation mechanism and kinematics of wind emission. As explained earlier, the value of the Br $\gamma$ /Br12 line ratio increases with decreasing optical depth. The spectral dependence of this ratio can help us distinguish between different wind components of different accelerations giving rise to the observed emission. In the earlier work of Drew, Bunn & Hoare (1993) and Bunn, Hoare & Drew (1995) ratios of Br $\alpha$ /Br $\gamma$  and Br $\alpha$ /Pf $\gamma$  were studied. Our Br $\gamma$ /Br12 ratios are expected to be comparable with those as the absorption cross sections of these lines have similar values to those of the lines they used (see also Lumsden et al. 2012).

The procedure for computing the ratios is as follows. We select a region of  $\pm 500$  km/s from the velocity center of the line, and rebin the spectra to correct for differences in resolution between the *K* and *H* bands. The extinction correction is applied and the continuum is fitted with a 2<sup>nd</sup> order polynomial fit and subtracted, and the two lines are divided. The chosen extinction value only affects the numerical value of the ratio, but that trends in shape of the ratio profile remain unchanged. A number of different features can be distinguished in the ratios, as shown in Figure 11. Some line ratio profiles show flat wings and a core, others a dish shaped profile. Central peaks are also seen, either narrow (FWHM $\approx$ 50–80 km/s) or wide (FWHM $\approx$ 80–100 km/s). Other objects display a central dip, blue or red asymmetries. Often two or more of these different types are all seen in a line ratio. Their relative proportions are shown in Table 3.

Some of these features have been seen in other line ratio surveys. Drew, Bunn & Hoare (1993) reported a dish shaped profile in S106IRS1 in their Br $\alpha$ /Br $\gamma$  spectral line ratio, which they interpret as an accelerated wind, while Lumsden et al. (2012) find a peaked shape in most of the Br $\gamma$ /Br12 ratios.

A dish shaped profile will indicate optically thin gas expanding faster than the optically thick central material. Drew, Bunn & Hoare (1993) also see a narrow central peak in the S106IRS1 ratio, which they interpret as an optically thin nebular gas region. They find single peaks in both Br $\alpha$  and Br $\gamma$ . We also see a single peak in Br $\gamma$ , but double peaked Br12. In addition to the wind, this could indicate the presence of a rotating disc. This is in agreement with radio observations of Gibb & Hoare (2007), who find an elongated structure, which they identify with an equatorial disk wind. However, the disk is probably not fully ionised given the detection of CO bandhead emission towards this object.

By the same logic, a weak and wide peak can be seen as an inverted dish shape, where the optically thin gas is expanding slower than the optically thick gas. We interpret this as a decelerating wind. A central dip within a wider peak can be seen as a decelerating wind combined with a larger, optically thick nebular region. A flat ratio simply shows all regions expanding at the same acceleration, irre-

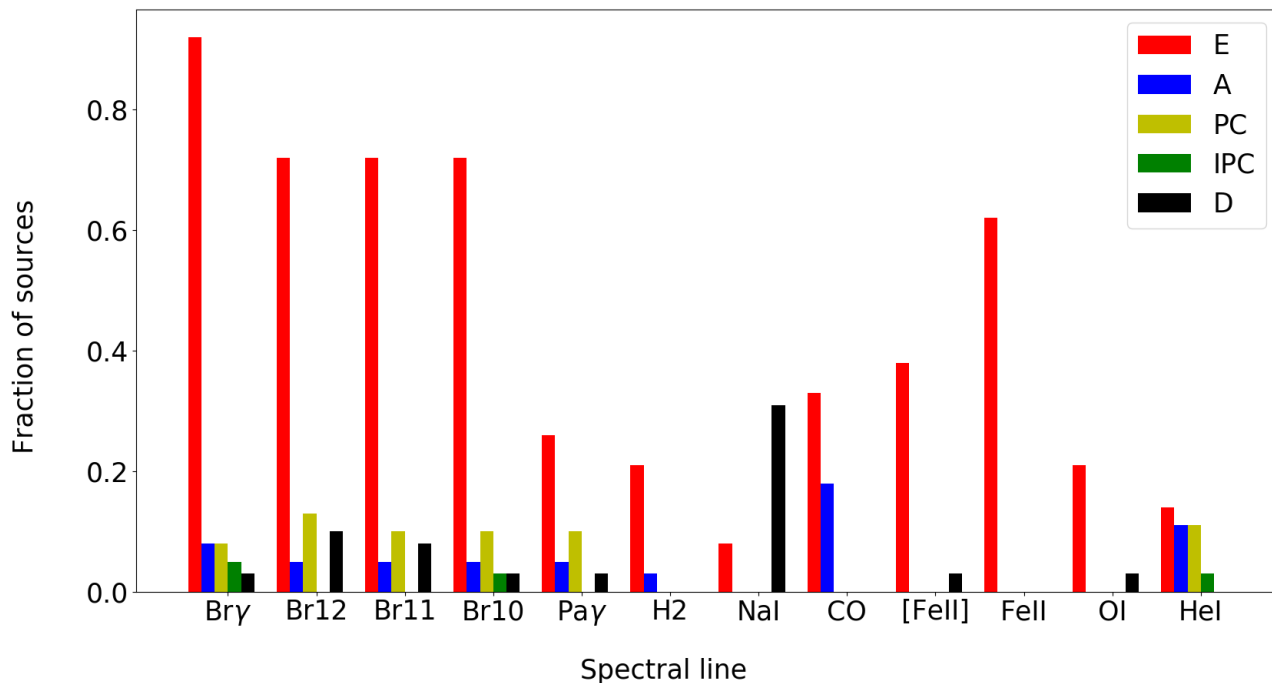


**Figure 8.** Detection rates of different features, with different profile types. E=single-peaked emission, A=absorption, PC=P Cygni profile, IPC=inverse P Cygni and D=double peaked

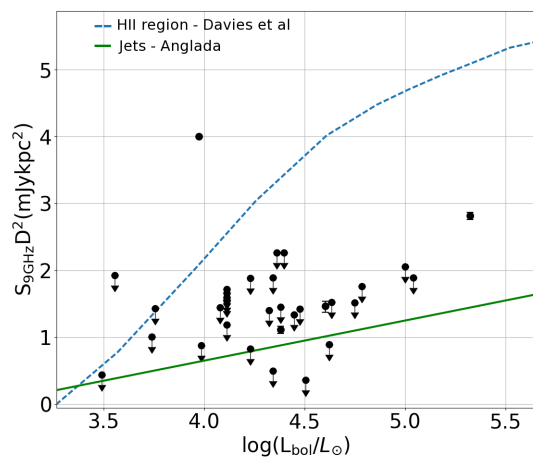


**Figure 9.** Radio flux at 9 GHz of our MYSOs, taken from the RMS database when available, as a function of bolometric luminosity. HII regions are expected to be found close to the dotted blue curve, as per the models of Davies et al. (2011), whereas MYSO jets closer to the green line, resulting from a fit to observations by Anglada (1995).

spective of optical thickness. Asymmetries are suggestive of infall (on the red side) or outflow (on the blue side).

Regarding any correlations between the HI ratio features and bolometric luminosity, we find that there is no clear trend between these two quantities. We also found no correlation with the Cooper (2013) MYSO Types 1-3, or with 2MASS NIR colours. This may be due to our small sample size. It is possible that with a distance-limited full sample such trends might appear. Still, it is interesting

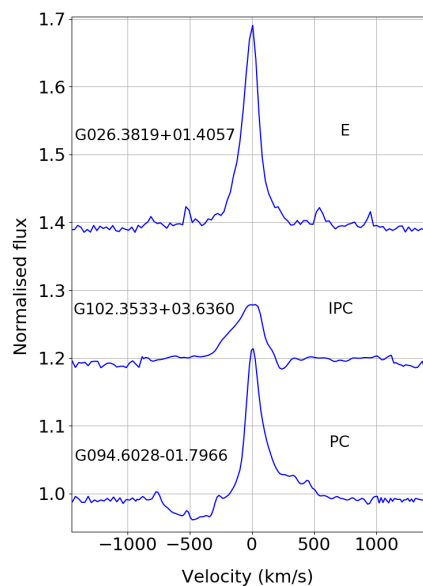


**Figure 10.** Examples of Br $\gamma$  profiles from our sample. From top to bottom: single-peaked emission G026.3819; inverse P Cygni absorption G102.3533; P Cygni absorption G094.6028

to note the variety of features observed. Following our presence of absorption lines in a number of our targets (see Section 4.2.2), we also investigated the effect of the photospheric absorption lines on the observed Br $\gamma$ /Br12 wind line ratios. The emission first fills in the photospheric absorption lines and arguably this needs to be taken into account in case the continuum excess emission is small.

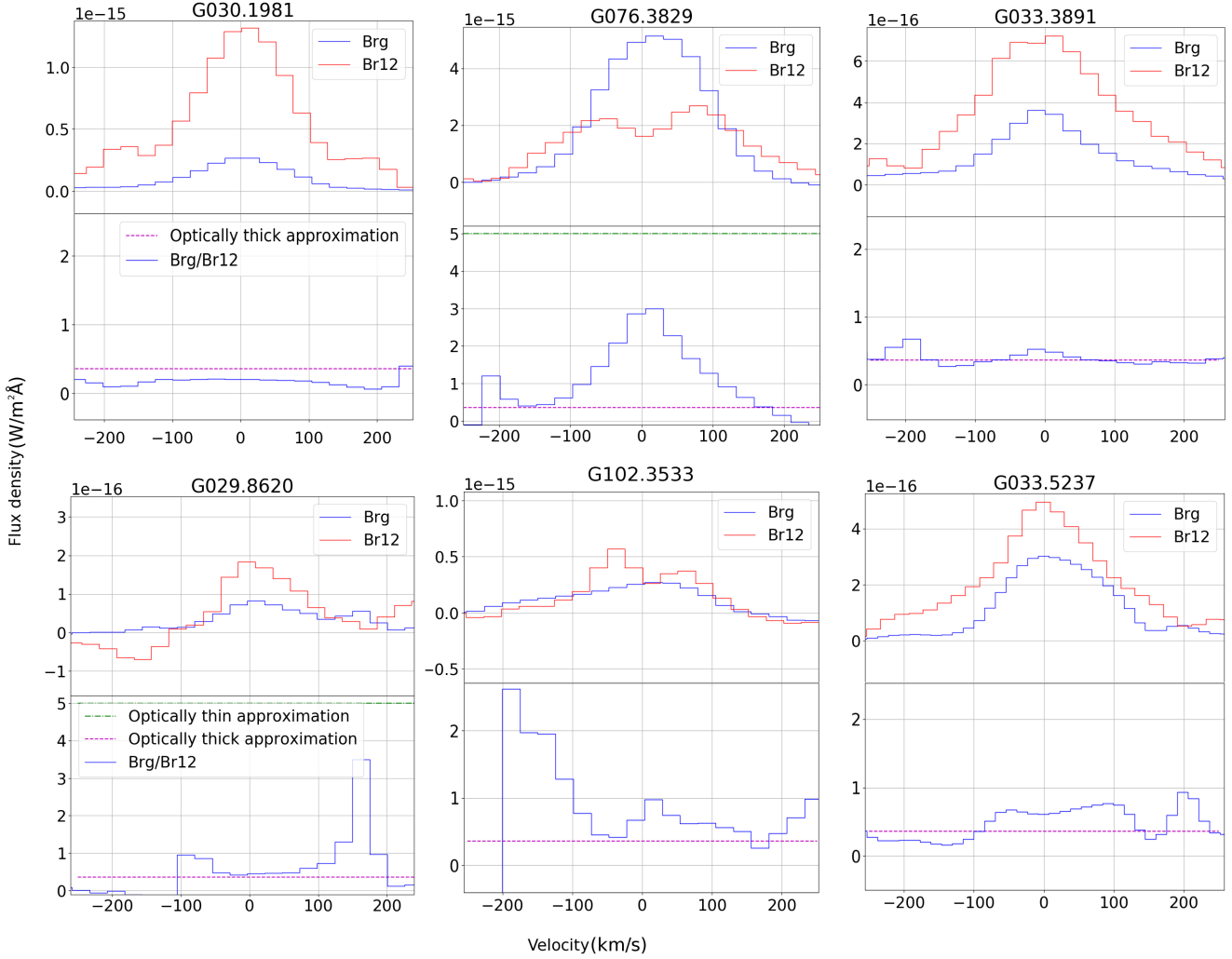


**Figure 11.** Examples of different types of profile ratio in  $\text{Br}\gamma/\text{Br}12$ . The horizontal axis denotes the velocity. Top (left to right): Flat ratio, Wide peak, Narrow peak. Bottom (left to right): Dish shape, Dish shape+central peak, Central dip.

We worked this out for a range of extinction and excess values and find that the effect induced by photospheric absorption lines will be less than 10% of the  $\text{Br}\gamma/\text{Br}12$  ratio value in the wings. We leave a detailed analysis of this effect for all our targets to a future study, but it is worth remembering that core features in the wind line ratios that are less than 10% of the wing value are likely caused by intrinsic photospheric absorption.

## 5 CONCLUSIONS

We have presented medium-resolution echelle NIR spectroscopic data for 36 MYSOs from the GNIRS instrument on the Gemini-North telescope<sup>2</sup>. Nearly a third of these constitute the first NIR spectra taken for these objects. This is the largest sample of MYSOs studied at this resolution at these wavelengths of MYSOs to date. Dust extinction is estimated from the slope of the continuum in the  $H$  band. Our main findings are as follows:

<sup>2</sup> **Note** - The spectral atlas with equivalent widths, line fluxes and luminosities as well as continuum-normalised full spectra are available as appendices which can be found only in the online version of this paper.

- We have found photospheric absorption lines for one object, G015.1288. These lines indicate that this source is best fit by a spectral type of A1b. An MYSO with an A supergiant configuration is consistent with the simulations of swollen up MYSOs of Hosokawa, Yorke & Omukai (2010) and Haemmerlé & Peters (2016).
- The accretion luminosities and rates from  $\text{Br}\gamma$  agree with results for lower mass sources, providing tentative evidence for a continuity of star formation processes across a large mass range.
- 75% of the lines of interest studied in this survey correlate with one another in terms of luminosity. This may be due to correlations with stellar luminosity.
- $\text{Br}\gamma/\text{Br}12$  line profile ratios show a wide variety of features, possibly corresponding to a range of winds. We see ratios corresponding to accelerated, constant or decelerated wind characteristics, as well as traces of wider regions of different optical thickness.
- We find no correlation between line ratio features and luminosity, NIR colours or MYSO Types cf. Cooper (2013)

## ACKNOWLEDGEMENTS

RP gratefully acknowledges the studentship funded by the Science and Technologies Facilities Council of the United Kingdom. We thank the anonymous referee for the comments and suggestions, which improved the quality of this article. This publication makes use of data products from the Two Micron All Sky Survey, which is a joint project of the University of Massachusetts and the Infrared Processing and Analysis Center/California Institute of Technology, funded by the National Aeronautics and Space Administration and the National Science Foundation. We also make use of the SIMBAD data base, operated at CDS, Strasbourg, France. This paper made use of information from the Red MSX Source survey database at [http://rms.leeds.ac.uk/cgi-bin/public/RMS\\_DATABASE.cgi](http://rms.leeds.ac.uk/cgi-bin/public/RMS_DATABASE.cgi) which was constructed with support from the Science and Technology Facilities Council of the UK. The reduction process made use of PyRAF, which is a product of the Space Telescope Science Institute, operated by AURA for NASA.

## REFERENCES

- Ababakr K. M., Oudmaijer R. D., Vink J. S., 2016, *MNRAS*, 461, 3089
- Anglada G., 1995, in *Revista Mexicana de Astronomía y Astrofísica*, vol. 27, Vol. 1, *Revista Mexicana de Astronomía y Astrofísica Conference Series*, Lizano S., Torrelles J. M., eds., p. 67
- Beltrán M. T., de Wit W. J., 2016, *A&ARv*, 24, 6
- Bertout C., 1989, *ARA&A*, 27, 351
- Bik A., Kaper L., Waters L. B. F. M., 2006, *Astronomy & Astrophysics*, 455, 561
- Blondel P. F. C., Djie H. R. E. T. A., 2006, *A&A*, 456, 1045
- Blum R. D., Barbosa C. L., Damineli A., Conti P. S., Ridgway S., 2004, *apj*, 617, 1167
- Bonnell I. A., Bate M. R., 2006, *Monthly Notices of the Royal Astronomical Society*, 370, 488
- Bonnell I. A., Bate M. R., Zinnecker H., 1998, *Monthly Notices of the Royal Astronomical Society*, 298, 93
- Bouvier J., Alencar S. H. P., Harries T. J., Johns-Krull C. M., Romanova M. M., 2007, *Protostars and Planets V*, 479
- Bunn J. C., Hoare M. G., Drew J. E., 1995, *Monthly Notices of the Royal Astronomical Society*, 272, 346
- Burton M. G., Lazendic J. S., Yusef-Zadeh F., Wardle M., 2004, *MNRAS*, 348, 638
- Cauley P. W., Johns-Krull C. M., 2015, *The Astrophysical Journal*, 810, 5
- Chandler C. J., Carlstrom J. E., Scoville N. Z., 1995, *The Astrophysical Journal*, 446, 793
- Cooper H. D. B., 2013, PhD thesis, University of Leeds
- Cooper H. D. B. et al., 2013, *Monthly Notices of the Royal Astronomical Society*, 430, 1125
- Cox N. L. J., Cami J., Kaper L., Ehrenfreund P., Foing B. H., Ochsendorf B. B., van Hooft S. H. M., Salama F., 2014, *A&A*, 569, A117
- Davies B., Hoare M. G., Lumsden S. L., Hosokawa T., Oudmaijer R. D., Urquhart J. S., Mottram J. C., Stead J., 2011, *Monthly Notices of the Royal Astronomical Society*, 416, 972
- Davies B., Lumsden S. L., Hoare M. G., Oudmaijer R. D., de Wit W.-J., 2010, *Monthly Notices of the Royal Astronomical Society*, 402, 1504
- Drew J. E., Bunn J. C., Hoare M. G., 1993, *Monthly Notices of the Royal Astronomical Society*, 265, 12
- Fairlamb J. R., Oudmaijer R. D., Mendigutía I., Ilee J. D., van den Ancker M. E., 2015, *MNRAS*, 453, 976
- Gibb A. G., Hoare M. G., 2007, *MNRAS*, 380, 246
- Haemmerlé L., Peters T., 2016, *Monthly Notices of the Royal Astronomical Society*, 458, 3299
- Hamano S. et al., 2015, *ApJ*, 800, 137
- Hanson M. M., Kudritzki R.-P., Kenworthy M. A., Puls J., Tokunaga A. T., 2005, *The Astrophysical Journal*, 161, 154
- Hinkle K. H., Wallace L., Livingston W., 1995, in *Astronomical Society of the Pacific Conference Series*, Vol. 81, *Laboratory and Astronomical High Resolution Spectra*, Sauval A. J., Blomme R., Grevesse N., eds., p. 66
- Hoare M. G., Franco J., 2007, *Astrophysics and Space Science Proceedings*, 1, 61
- Hosokawa T., Yorke H. W., Omukai K., 2010, *The Astrophysical Journal*, 721, 478
- Ilee J. D., Fairlamb J., Oudmaijer R. D., Mendigutía I., van den Ancker M. E., Kraus S., Wheelwright H. E., 2014, *Monthly Notices of the Royal Astronomical Society*, 445, 3723
- Ilee J. D. et al., 2013, *Monthly Notices of the Royal Astronomical Society*, 429, 2960
- Kahn F. D., 1974, *Astronomy & Astrophysics*, 37, 149
- Kendall T. R., de Wit W. J., Yun J. L., 2003, *Astronomy and Astrophysics*, 408, 313
- Kraus S. et al., 2010, *Nature*, 466, 339
- Krumholz M. R., Klein R. I., McKee C. F., Offner S. S. R., Cunningham A. J., 2009, *Science*, 323, 754
- Lucas P. W. et al., 2008, *Monthly Notices of the Royal Astronomical Society*, 391, 136
- Lumsden S. L., Hoare M. G., 1996, *APj*, 464, 272
- Lumsden S. L., Hoare M. G., Urquhart J. S., Oudmaijer R. D., Davies B., Mottram J. C., Cooper H. D. B., Moore T. J. T., 2013, *The Astrophysical Journals*, 208, 11
- Lumsden S. L., Wheelwright H. E., Hoare M. G., Oudmaijer R. D., Drew J. E., 2012, *Monthly Notices of the Royal Astronomical Society*, 424, 1088
- Martin P. G., Whittet D. C. B., 1990, *The Astrophysical Journal*, 357, 113
- Mendigutía I., Calvet N., Montesinos B., Mora A., Muzerolle J., Eiroa C., Oudmaijer R. D., Merín B., 2011, *Astronomy & Astrophysics*, 535, A99
- Mendigutía I., Oudmaijer R. D., Rigliaco E., Fairlamb J. R., Calvet N., Muzerolle J., Cunningham N., Lumsden S. L., 2015, *Monthly Notices of the Royal Astronomical Society*, 452, 2837
- Meyer M. R., Edwards S., Hinkle K. H., Strom S. E., 1998, *The Astrophysical Journal*, 508, 397
- Moore T. J. T., Lumsden S. L., Ridge N. A., Puxley P. J., 2005, *MNRAS*, 359, 589
- Mottram J. C. et al., 2011, *Astronomy & Astrophysics*, 525, A149
- Mottram J. C., Vink J. S., Oudmaijer R. D., Patel M., 2007, *MNRAS*, 377, 1363
- Natta A., Testi L., Randich S., 2006, *Astronomy and Astrophysics*, 452, 245
- Oudmaijer R. D., Busfield G., Drew J. E., 1997, *MNRAS*, 291, 797
- Oudmaijer R. D., de Wit W.-J., 2014, in *EAS Publications Series*, Vol. 69, *EAS Publications Series*, pp. 319–331
- Porter J. M., Drew J. E., Lumsden S. L., 1998, *Astronomy & Astrophysics*, 332, 999
- Purser S. J. D. et al., 2016, *MNRAS*, 460, 1039
- Rosen A. L., Krumholz M. R., McKee C. F., Klein R. I., 2016, *Monthly Notices of the Royal Astronomical Society*, 463, 2553

- Rosero V. et al., 2016, *Apjs*, 227, 25
- Salpeter E. E., 1955, *The Astrophysical Journal*, 121, 161
- Science Software Branch at STScI, 2012, PyRAF: Python alternative for IRAF. Astrophysics Source Code Library
- Shu F. H., Adams F. C., Lizano S., 1987, *Astronomy & Astrophysics Reviews*, 25, 23
- Simon M., Righini-Cohen G., Cassar L., Fischer J., 1981, *The Astrophysical Journal*, 251, 552
- Skrutskie M. F. et al., 2006, *The Astronomical Journal*, 131, 1163
- Straizys V., Kuriliene G., 1981, *Astrophysics and space science*, 80, 353
- Urquhart J. S. et al., 2009, *Astronomy & Astrophysics*, 501, 539
- Urquhart J. S. et al., 2011a, *Monthly Notices of the Royal Astronomical Society*, 410, 1237
- Urquhart J. S. et al., 2011b, *Monthly Notices of the Royal Astronomical Society*, 418, 1689
- Wheelwright H. E., Oudmaijer R. D., de Wit W. J., Hoare M. G., Lumsden S. L., Urquhart J. S., 2010, *Monthly Notices of the Royal Astronomical Society*, 408, 1840

**Table 1.** Spectral atlas, with equivalent widths in Å, fluxes uncorrected for extinction and in W/m<sup>2</sup>Å and luminosities in L<sub>⊙</sub>

Object	Upper limit EW	EW <sub>Brγ</sub>	ΔEW <sub>Brγ</sub>	F <sub>Brγ</sub>	dF <sub>Brγ</sub>	L <sub>Brγ</sub>	Δ L <sub>Brγ</sub>	L <sub>Acc</sub>	Δ L <sub>Acc</sub>	M	Δ M	R	Δ R	$\dot{M}$	Δ $\dot{M}$
G010.8411-02.5919	0.09	-0.6	0.2	5.4E-18	1.4E-18	1.5E-01	4.1E-02	6.5E+02	1.8E+02	15.9	0.8	6.0	0.3	7.9E-06	3.9E-07
G010.8856+00.1221	0.10	-1.8	0.2	1.1E-17	1.0E-18	5.9E-01	1.6E-01	2.2E+03	5.9E+02	10.5	0.5	2.9	0.1	1.9E-05	9.7E-07
G012.9090-00.2607	0.11	-2.3	0.2	2.1E-17	1.7E-18	1.0E-01	2.7E-02	4.5E+02	1.2E+02	17.2	0.9	6.9	0.3	4.5E-03	2.2E-04
G014.9958-00.6732	0.07	-18.1	0.1	9.6E-16	6.2E-18	8.0E+00	2.1E+00	2.3E+04	6.2E+03	13.4	0.7	4.4	0.2	2.4E-04	1.2E-05
G015.1288-00.6717	0.05	-1.9	0.1	2.3E-17	1.0E-18	4.1E-02	1.1E-02	2.0E+02	5.3E+01	13.1	0.7	4.2	0.2	2.1E-06	1.0E-07
G017.6380+00.1566	0.01	-0.6	0.0	2.9E-17	1.3E-18	4.4E-02	1.2E-02	1.5E+02	4.1E+01	8.5	0.2	3.2	0.1	3.1E-05	8.4E-07
G018.3412+00.1566	0.06	-2.3	0.1	1.9E-17	8.0E-19	1.4E+00	3.7E-01	4.8E+03	1.3E+03	15.5	0.8	5.7	0.3	5.7E-05	2.9E-06
G023.3891+00.1851	0.08	-0.3	0.1	5.3E-18	2.3E-18	5.7E-01	1.5E-01	2.1E+03	5.8E+02	15.9	0.8	6.0	0.3	2.6E-05	1.3E-06
G025.4118+00.1052A	0.18														
G026.2020+00.2262	0.07	-3.5	0.1	7.0E-17	2.3E-18	7.1E+00	1.9E+00	2.1E+04	5.5E+03	9.4	0.5	2.3	0.1	1.7E-04	8.3E-06
G026.3819+01.4057	0.05	-3.8	0.1	3.5E-17	8.5E-19	3.5E-01	9.5E-02	1.4E+03	3.7E+02	14.4	0.7	5.1	0.3	1.6E-05	7.9E-07
G027.7571+00.0500	0.11	-2.4	0.2	1.9E-17	1.5E-18	1.0E+01	2.7E+00	2.9E+04	7.7E+03	13.4	0.7	4.4	0.2	3.0E-04	1.5E-05
G029.8620-00.0444	0.07	-1.9	0.1	1.3E-17	8.0E-19	7.3E-01	2.0E-01	2.7E+03	7.2E+02	16.6	0.8	6.5	0.3	3.4E-05	1.7E-06
G030.1981-00.1691	0.06	-1.1	0.1	1.0E-17	8.6E-19	2.0E+00	5.4E-01	6.7E+03	1.8E+03	16.9	0.8	6.7	0.3	8.6E-05	4.3E-06
G033.3891+00.1989	0.07	-2.1	0.2	1.3E-16	9.9E-18	3.2E+00	8.7E-01	1.0E+04	2.8E+03	13.4	0.7	4.4	0.2	1.1E-04	5.5E-06
G033.5237+00.0198	0.07	-2.9	0.1	4.9E-17	2.0E-18	6.7E+00	1.8E+00	2.0E+04	5.3E+03	13.4	0.7	4.4	0.2	2.1E-04	1.1E-05
G034.0500-00.2977_A	0.08	-3.6	0.1	3.3E-17	1.3E-18	1.1E+00	3.0E-01	3.9E+03	1.0E+03	15.7	0.8	5.9	0.3	4.7E-05	2.4E-06
G034.0500-00.2977_B	0.08	-4.7	0.1	1.3E-16	4.0E-18	4.4E+00	1.2E+00	1.4E+04	3.6E+03	15.7	0.8	5.9	0.3	1.6E-04	8.2E-06
G034.7123-00.5946	0.06	-0.1	0.1	1.9E-18	1.4E-18	1.7E-01	4.6E-02	7.3E+02	2.0E+02	12.3	0.6	3.8	0.2	7.3E-06	3.6E-07
G056.4120-00.0277	0.05	-2.2	0.1	5.3E-17	2.3E-18	4.0E+00	1.1E+00	1.2E+04	3.4E+03	15.5	0.8	5.7	0.3	1.5E-04	7.5E-06
G073.6525+00.1944	0.14	-1.2	0.2	6.6E-18	1.3E-18	8.4E-01	2.3E-01	3.0E+03	8.2E+02	23.7	1.2	12.3	0.6	5.1E-05	2.5E-06
G073.6952-00.9996	0.12	-2.5	0.2	5.7E-17	4.5E-18	1.8E+01	4.9E+00	4.8E+04	1.3E+04	14.4	0.7	5.1	0.3	5.5E-04	2.7E-05
G076.3829-00.6210	0.08	-15.0	0.1	2.8E-15	2.4E-17	4.8E+00	1.3E+00	1.5E+04	3.9E+03	18.4	0.9	7.7	0.4	2.0E-04	1.0E-05
G077.4622+01.7600	0.12	-0.4	0.2	3.9E-18	2.1E-18	1.9E-02	5.2E-03	1.0E+02	2.7E+01	9.0	0.4	2.2	0.1	7.9E-07	3.9E-08
G078.8867+00.7087	0.08	0.3	-0.1	2.5E-17	1.3E-17	8.6E-02	2.3E-02								
G094.3228-00.1671	0.11	-19.2	0.2	1.2E-16	1.2E-18	9.5E+00	2.6E+00	2.7E+04	7.2E+03	18.7	0.9	8.0	0.4	3.7E-04	1.9E-05
G094.6028-01.7966	0.08	-3.2	0.1	2.8E-16	1.2E-17	4.4E+00	1.2E+00	1.4E+04	3.6E+03	10.6	0.5	2.9	0.1	1.2E-04	6.0E-06
G102.3533+03.6360	0.06	-1.4	0.1	9.8E-17	6.7E-18	1.2E+01	3.1E+00	3.2E+04	8.7E+03	24.4	1.2	12.8	0.6	5.5E-04	2.8E-05
G106.7968+05.3121	0.05	-1.2	0.1	7.9E-17	5.4E-18	2.0E-02	5.4E-03	5.6E+01	1.5E+01	7.7	0.2	4.1	0.1	1.8E-04	4.7E-06
G110.1082+00.0473B_A	0.16														
G110.1082+00.0473B_B	0.04	-4.0	0.1	6.8E-17	1.8E-18	1.3E-02	3.4E-03	7.0E+01	1.9E+01	12.2	0.6	3.8	0.2	6.9E-07	3.5E-08
G111.2348-01.2385	0.35	-1.4	0.6	1.0E-17	4.3E-18	1.3E+01	3.6E+00	3.6E+04	9.7E+03	18.6	0.9	7.9	0.4	5.0E-04	2.5E-05
G111.5234+00.8004A	0.05	-2.4	0.1	8.3E-17	3.2E-18	7.2E-01	1.9E-01	2.6E+03	7.0E+02	20.2	1.0	9.2	0.5	3.9E-05	1.9E-06
G111.5423+00.7776	0.19	-5.1	0.3	8.8E-17	5.8E-18	3.6E+02	9.7E+01	7.0E+05	1.9E+05	29.2	1.5	17.8	0.9	1.4E-02	6.9E-04
G120.1483+03.3745	0.05	-3.5	0.3	2.9E-16	2.3E-17	8.1E+00	2.2E+00	2.3E+04	6.3E+03	15.3	0.8	5.6	0.3	2.8E-04	1.4E-05
G151.6120-00.4575	0.09	-3.1	0.2	2.4E-16	1.2E-17	4.4E+00	1.2E+00	1.3E+04	3.6E+03	20.7	1.0	9.6	0.5	2.0E-04	1.0E-05
G213.7040-12.5971_A	0.03	-1.2	0.1	5.3E-18	2.7E-19	1.5E-03	4.1E-04	3.7E+00	9.9E-01	7.5	0.2	2.5	0.1	6.2E-04	1.7E-05
G213.7040-12.5971_B	0.01	-0.4	0.1	1.7E-18	8.4E-20	4.7E-04	1.3E-04	1.2E+00	3.1E-01	7.5	0.2	2.5	0.1	6.2E-04	1.7E-05
G233.8306-00.1803A	0.10	-17.4	0.2	2.4E-15	2.5E-17	4.2E+01	1.1E+01	1.0E+05	2.8E+04	13.4	0.7	4.4	0.2	1.1E-03	5.5E-05

**Table 2.** Spectral atlas, with equivalent widths in Å, fluxes uncorrected for extinction and in  $\text{W/m}^2\text{Å}$  and luminosities in  $L_{\odot}$ 

Object	$\text{EW}_{CO}$	$\Delta\text{EW}_{CO}$	$F_{CO}$	$\Delta F_{CO}$	$L_{CO}$	$\Delta L_{CO}$	$\text{EW}_{Br12}$	$\Delta\text{EW}_{Br12}$	$F_{Br12}$	$\Delta F_{Br12}$	$L_{Br12}$	$\Delta L_{Br12}$
G010.8411-02.5919												
G010.8856+00.1221							-0.5	0.1	3.5E-19	3.3E-20	3.5E-01	1.3E-01
G012.9090-00.2607	-5.5	0.3	1.2E-16	5.2E-18	7.0E+02	6.0E+01						
G014.9958-00.6732							-12.5	0.1	1.6E-16	1.1E-18	1.1E+01	4.3E+00
G015.1288-00.6717							3.0	0.1	-2.4E-17	8.1E-19	1.5E-01	5.8E-02
G017.6380+00.1566												
G018.3412+00.1566							-1.7	0.1	1.1E-18	4.5E-20	5.3E+00	2.1E+00
G023.3891+00.1851							-2.2	0.9	5.6E-18	2.4E-18	1.6E-01	6.1E-02
G025.4118+00.1052A												
G026.2020+00.2262							-2.2	0.1	1.2E-17	3.8E-19	9.4E+00	4.1E+00
G026.3819+01.4057							-2.7	0.1	1.3E-17	3.2E-19	7.6E-01	3.0E-01
G027.7571+00.0500							-1.4	0.1	8.5E-19	6.7E-20	1.2E+01	4.6E+00
G029.8620-00.0444							-1.3	0.1	1.2E-18	7.5E-20	9.4E-01	4.3E-01
G030.1981-00.1691							-2.6	0.2	7.7E-18	6.4E-19	9.8E+00	3.8E+00
G033.3891+00.1989	-2.6	0.1	1.7E-16	9.4E-18	5.6E+00	2.7E-01	-3.1	0.2	4.1E-17	3.1E-18	8.0E+00	3.1E+00
G033.5237+00.0198							-1.9	0.1	3.7E-18	1.5E-19	7.2E+00	2.8E+00
G034.0500-00.2977_A							7.3	0.3	-1.2E-16	4.6E-18	3.6E+00	1.6E+00
G034.0500-00.2977_B							-2.1	0.1	3.4E-17	1.0E-18	5.2E+00	2.3E+00
G034.7123-00.5946	-1.1	0.7	1.6E-17	1.1E-17	2.8E+00	1.7E+00						
G056.4120-00.0277	-1.4	0.1	3.9E-17	1.5E-18	3.6E+00	1.4E-01	-1.3	0.1	1.4E-17	5.8E-19	6.2E+00	2.4E+00
G073.6525+00.1944	-5.3	0.8	3.6E-17	6.3E-18	5.1E+00	7.6E-01	-3.6	0.7	1.1E-17	2.2E-18	5.8E+00	2.2E+00
G073.6952-00.9996	-3.4	0.2	1.2E-16	7.1E-18	4.0E+01	4.9E+00	-0.5	0.1	2.7E-18	5.3E-19	1.1E+01	4.1E+00
G076.3829-00.6210	-4.7	0.5	9.5E-16	7.4E-18	2.0E+00	1.2E-01	-2.8	0.2	3.1E-16	2.2E-17	2.4E+00	9.5E-01
G077.4622+01.7600							-1.4	0.7	1.5E-17	7.7E-18	2.9E-01	1.1E-01
G078.8867+00.7087							-1.5	0.8	5.6E-18	3.0E-18	1.9E-02	1.0E-02
G094.3228-00.1671							-8.5	0.1	1.5E-17	1.5E-19	1.7E+01	6.8E+00
G094.6028-01.7966	-5.7	0.1	5.8E-16	2.3E-17	1.08E+01	3.3E-01	-1.2	0.1	4.4E-17	3.8E-18	2.2E+00	9.4E-01
G102.3533+03.6360							-0.4	0.1	6.7E-18	1.6E-18	6.9E+00	2.7E+00
G106.7968+05.3121	-3.4	-0.1	8.8E-16	3.3E-17	7.1E-02	2.7E-03						
G110.1082+00.0473B_A												
G110.1082+00.0473B_B							-0.2	0.1	2.7E-18	1.4E-18	2.0E-03	7.7E-04
G111.2348-01.2385												
G111.5234+00.8004A							-0.7	0.1	1.0E-17	1.5E-18	5.4E-01	2.1E-01
G111.5423+00.7776												
G120.1483+03.3745							-2.3	0.2	6.4E-17	5.1E-18	1.2E+01	4.6E+00
G151.6120-00.4575	-2.8	0.1	3.8E-16	1.4E-17	5.8E+00	1.5E-01	-1.3	0.1	4.4E-17	2.2E-18	3.8E+00	1.5E+00
G213.7040-12.5971_A							-0.8	0.1	1.4E-18	6.8E-20	3.8E-04	1.9E-05
G213.7040-12.5971_B							-0.7	0.1	1.2E-18	6.0E-20	3.4E-04	1.7E-05
G233.8306-00.1803A							-8.9	0.1	5.9E-16	6.1E-18	5.9E+01	2.3E+01

**Table 3.** Spectral atlas, with equivalent widths in Å, fluxes uncorrected for extinction and in W/m<sup>2</sup>Å and luminosities in L<sub>⊙</sub>

Object	EW <sub>Br11</sub> (Å)	ΔEW <sub>Br11</sub>	F <sub>Br11</sub>	Δ F <sub>Br11</sub>	L <sub>Br11</sub>	Δ L <sub>Br11</sub>	EW <sub>Br10</sub>	ΔEW <sub>Br10</sub>	F <sub>Br10</sub>	Δ F <sub>Br10</sub>	L <sub>Br10</sub>	Δ L <sub>Br10</sub>
G010.8411-02.5919												
G010.8856+00.1221	-0.5	0.2	3.8E-19	1.5E-19	4.5E-01	1.8E-01	-0.1	0.1	1.5E-19	6.0E-20	6.6E-01	2.6E-01
G012.9090-00.2607												
G014.9958-00.6732	-13.7	5.3	1.8E-16	7.1E-17	1.3E+01	5.2E+00	-17.2	6.7	2.8E-16	1.1E-16	1.4E+01	5.6E+00
G015.1288-00.6717	2.7	1.0	1.8E-17	7.0E-18	1.5E-01	6.0E-02	3.4	1.3	2.4E-17	9.4E-18	2.4E-01	9.5E-02
G017.6380+00.1566												
G018.3412+00.1566	-2.0	0.8	1.5E-18	6.0E-19	7.9E+00	3.1E+00	-1.7	0.7	1.9E-18	7.3E-19	1.4E+01	5.5E+00
G023.3891+00.1851	-0.7	0.3	1.8E-18	7.0E-19	6.4E-02	2.5E-02	-0.7	0.3	2.4E-18	9.3E-19	9.2E-02	3.6E-02
G025.4118+00.1052A												
G026.2020+00.2262	-2.3	1.0	1.5E-17	6.4E-18	1.4E+01	6.1E+00	-2.6	1.2	1.9E-17	8.4E-18	2.0E+01	9.0E+00
G026.3819+01.4057	-3.1	1.2	1.6E-17	6.3E-18	1.0E+00	4.0E-01	-2.6	1.0	1.5E-17	5.7E-18	1.1E+00	4.3E-01
G027.7571+00.0500	-1.8	0.7	1.7E-18	6.5E-19	2.4E+01	9.3E+00	-1.8	0.7	2.8E-18	1.1E-18	3.8E+01	1.5E+01
G029.8620-00.0444	-1.6	0.7	1.8E-18	8.2E-19	1.4E+00	6.2E-01	-1.1	0.5	1.6E-18	7.3E-19	1.7E+00	7.8E-01
G030.1981-00.1691	-11.1	4.3	1.1E-17	4.3E-18	1.1E+01	4.4E+00	-7.0	2.7	9.7E-18	3.8E-18	1.4E+01	5.4E+00
G033.3891+00.1989	-2.5	1.0	3.8E-17	1.5E-17	8.6E+00	3.3E+00	-2.2	0.9	4.0E-17	1.5E-17	9.4E+00	3.7E+00
G033.5237+00.0198	-2.9	1.1	5.1E-18	2.0E-18	1.2E+01	4.5E+00	-2.8	1.1	6.6E-18	2.6E-18	2.2E+01	8.4E+00
G034.0500-00.2977.A	5.2	2.2	7.5E-17	3.2E-17	3.0E+00	1.3E+00	4.6	2.0	6.3E-17	2.7E-17	3.6E+00	1.5E+00
G034.0500-00.2977.B	-2.6	1.1	4.0E-17	1.7E-17	5.7E+00	2.5E+00	-5.6	2.4	8.7E-17	3.7E-17	1.4E+01	6.2E+00
G034.7123-00.5946												
G056.4120-00.0277	-1.4	0.5	1.6E-17	6.1E-18	7.0E+00	2.7E+00	-1.1	0.4	1.6E-17	6.3E-18	7.6E+00	3.0E+00
G073.6525+00.1944	-0.4	0.1	9.5E-19	3.7E-19	6.4E-01	2.5E-01	-0.4	0.2	1.2E-18	4.8E-19	9.6E-01	3.7E-01
G073.6952-00.9996	-0.9	0.4	6.1E-18	2.4E-18	2.5E+01	9.7E+00	-0.4	0.2	3.1E-18	1.2E-18	1.4E+01	5.3E+00
G076.3829-00.6210	-4.4	1.7	3.9E-16	1.5E-16	2.6E+00	1.0E+00	-4.2	1.6	4.2E-16	1.6E-16	4.0E+00	1.5E+00
G077.4622+01.7600	-1.6	0.6	9.9E-18	3.8E-18	3.5E-01	1.3E-01	-0.5	0.2	3.8E-18	1.5E-18	1.7E-01	6.5E-02
G078.8867+00.7087												
G094.3228-00.1671	-9.9	3.9	1.8E-17	7.0E-18	2.6E+01	1.0E+01	-12.0	4.7	2.7E-17	1.1E-17	4.0E+01	1.6E+01
G094.6028-01.7966	-1.7	0.7	3.7E-17	1.6E-17	2.8E+00	1.2E+00	-1.5	0.6	3.6E-17	1.5E-17	3.2E+00	1.3E+00
G102.3533+03.6360	-0.6	0.2	8.8E-18	3.4E-18	8.2E+00	3.2E+00	-0.8	0.3	1.5E-17	5.8E-18	9.5E+00	3.7E+00
G106.7968+05.3121												
G110.1082+00.0473B.A	-0.2	0.1	1.1E-18	5.4E-19	1.3E-03	5.1E-04	-0.3	0.1	3.8E-18	1.1E-18	4.6E-03	1.8E-03
G110.1082+00.0473B.B	-0.5	0.2	4.2E-18	1.6E-18	3.3E-03	1.3E-03	-0.8	0.3	7.0E-18	2.7E-18	7.1E-03	2.8E-03
G111.2348-01.2385												
G111.5234+00.8004A	-0.9	0.4	1.4E-17	5.4E-18	8.2E-01	3.2E-01	-1.3	0.5	2.2E-17	8.7E-18	1.1E+00	4.2E-01
G111.5423+00.7776												
G120.1483+03.3745	-2.9	1.1	7.8E-17	3.0E-17	1.7E+01	6.5E+00	-3.5	1.4	1.0E-16	4.0E-17	2.8E+01	1.1E+01
G151.6120-00.4575	-1.9	0.7	5.5E-17	2.1E-17	4.8E+00	1.9E+00	-1.7	0.7	5.2E-17	2.0E-17	3.8E+00	1.5E+00
G213.7040-12.5971.A	-0.9	0.3	1.9E-18	7.4E-19	5.4E-04	2.1E-04	-0.6	0.2	1.9E-18	7.2E-19	5.2E-04	2.0E-04
G213.7040-12.5971.B	-0.5	0.2	1.1E-18	4.1E-19	3.0E-04	1.2E-04	-0.6	0.2	1.3E-18	4.9E-19	3.6E-04	1.4E-04
G233.8306-00.1803A	-9.8	3.8	6.8E-16	2.7E-16	7.1E+01	2.8E+01	-12.6	4.9	9.9E-16	3.8E-16	1.2E+02	4.7E+01

**Table 4.** Spectral atlas, with equivalent widths in Angstroms, fluxes uncorrected for extinction and in  $\text{W/m}^2 \text{ \AA}$  and luminosities in solar luminosities

Object	$\text{EW}_{NaI}$	$\Delta \text{EW}_{NaI}$	$F_{NaI}$	$\Delta F_{NaI}$	$L_{NaI}$	$\Delta L_{NaI}$	$\text{EW}_{H_2}$	$\Delta \text{EW}_{H_2}$	$F_{H_2}$	$\Delta F_{H_2}$	$L_{H_2}$	$\Delta L_{H_2}$
G010.8411-02.5919												
G010.8856+00.1221												
G012.9090-00.2607	-0.5	0.2	7.7E-18	2.1E-18	5.1E+01	1.4E+01						
G014.9958-00.6732							-0.2	0.1	1.4E-17	5.5E-18	1.8E-03	6.9E-04
G015.1288-00.6717												
G017.6380+00.1566												
G018.3412+00.1566												
G023.3891+00.1851												
G025.4118+00.1052A												
G026.2020+00.2262	-0.1	0.0	2.0E-18	5.5E-19	2.3E-01	6.3E-02						
G026.3819+01.4057												
G027.7571+00.0500	-0.7	0.2	6.5E-18	1.8E-18	3.6E+00	9.7E-01						
G029.8620-00.0444	-0.4	0.1	4.3E-18	1.2E-18	1.7E-01	4.6E-02						
G030.1981-00.1691												
G033.3891+00.1989	-0.4	0.1	2.7E-17	7.2E-18	5.9E-01	1.6E-01						
G033.5237+00.0198	-0.3	0.1	5.1E-18	1.4E-18	8.1E-01	2.2E-01						
G034.0500-00.2977_A	-0.1	0.0	2.5E-18	6.8E-19	3.9E-02	1.1E-02						
G034.0500-00.2977_B	-0.2	0.1	3.8E-18	1.0E-18	1.8E-01	4.9E-02						
G034.7123-00.5946	-0.5	0.1	4.6E-18	1.2E-18	7.5E-01	2.0E-01						
G056.4120-00.0277	-0.2	0.1	9.7E-18	2.6E-18	4.0E-01	1.1E-01						
G073.6525+00.1944	-0.2	0.1	2.7E-18	7.2E-19	1.3E-01	3.5E-02						
G073.6952-00.9996	-0.3	0.1	8.9E-18	2.4E-18	2.3E+00	6.2E-01						
G076.3829-00.6210	-0.7	0.2	1.6E-16	4.3E-17	2.4E-01	6.4E-02						
G077.4622+01.7600												
G078.8867+00.7087	-0.2	0.1	2.0E-17	5.2E-18	1.1E-02	3.0E-03						
G094.3228-00.1671							-0.3	0.1	2.2E-18	8.4E-19	1.3E-03	5.1E-04
G094.6028-01.7966	-0.6	0.2	5.5E-17	1.5E-17	9.4E-01	2.5E-01						
G102.3533+03.6360												
G106.7968+05.3121	-0.5	0.1	5.9E-17	1.6E-17	1.5E-02	4.0E-03						
G110.1082+00.0473B_A												
G110.1082+00.0473B_B	-0.2	0.1	8.4E-15	2.3E-15	6.5E-04	1.8E-04						
G111.2348-01.2385	-0.9	0.2	9.2E-18	2.5E-18	9.5E+00	2.6E+00						
G111.5234+00.8004A												
G111.5423+00.7776												
G120.1483+03.3745												
G151.6120-00.4575												
G213.7040-12.5971_A												
G213.7040-12.5971_B							-0.1	0.1	7.4E-19	2.9E-19	2.1E-05	8.1E-06
G233.8306-00.1803A												

**Table 5.** Spectral atlas, with equivalent widths in Å, fluxes uncorrected for extinction and in W/m<sup>2</sup>Å and luminosities in L<sub>⊙</sub>

Object	EW <sub>HeI</sub>	ΔEW <sub>HeI</sub>	F <sub>HeI</sub>	Δ F <sub>HeI</sub>	L <sub>HeI</sub>	Δ L <sub>HeI</sub>	EW <sub>OI</sub>	ΔEW <sub>OI</sub>	F <sub>OI</sub>	Δ F <sub>OI</sub>	L <sub>OI</sub>	Δ L <sub>OI</sub>
G010.8411-02.5919												
G010.8856+00.1221												
G012.9090-00.2607												
G014.9958-00.6732							-15.5	4.2	1.1E-16	5.6E-18	2.6E+02	1.3E+01
G015.1288-00.6717	7.1	0.3	4.3E-18	1.9E-19	5.3E-04	1.4E-04						
G017.6380+00.1566												
G018.3412+00.1566												
G023.3891+00.1851												
G025.4118+00.1052A												
G026.2020+00.2262												
G026.3819+01.4057												
G027.7571+00.0500												
G029.8620-00.0444												
G030.1981-00.1691												
G033.3891+00.1989												
G033.5237+00.0198												
G034.0500-00.2977_A	1.7	0.1	7.8E-18	3.1E-19	4.0E-02	1.1E-02						
G034.0500-00.2977_B	-0.4	0.0	1.2E-18	3.6E-20	6.3E-03	1.7E-03	-3.9	1.0	5.2E-17	2.6E-18	1.7E+01	8.4E-01
G034.7123-00.5946												
G056.4120-00.0277	10.0	0.4	9.4E-18	4.1E-19	2.5E-02	6.8E-03						
G073.6525+00.1944												
G073.6952-00.9996												
G076.3829-00.6210												
G077.4622+01.7600												
G078.8867+00.7087												
G094.3228-00.1671												
G094.6028-01.7966	15.9	0.7	7.3E-17	3.1E-18	5.5E-02	1.5E-02	-1.4	0.4	2.0E-17	1.0E-18	3.8E+00	1.9E-01
G102.3533+03.6360												
G106.7968+05.3121												
G110.1082+00.0473B_A												
G110.1082+00.0473B_B	-4.9	0.1	4.0E-17	1.1E-18	2.3E-02	6.2E-03	-0.2	0.1	1.3E-18	6.5E-20	7.0E-03	3.5E-04
G111.2348-01.2385												
G111.5234+00.8004A							-2.6	0.7	3.4E-17	1.7E-18	1.5E+01	7.5E-01
G111.5423+00.7776												
G120.1483+03.3745							-1.7	0.5	1.1E-17	5.3E-19	3.1E+02	1.6E+01
G151.6120-00.4575	9.0	0.5	6.0E-17	3.0E-18	7.6E-02	2.1E-02						
G213.7040-12.5971_A												
G213.7040-12.5971_B												
G233.8306-00.1803A							-5.3	1.4	1.2E-17	6.0E-19	1.4E+03	6.8E+01

**Table 6.** Spectral atlas, with equivalent widths in Å, fluxes uncorrected for extinction and in  $\text{W/m}^2\text{Å}$  and luminosities in  $L_{\odot}$ 

Object	$\text{EW}_{Pa\gamma}$	$\Delta\text{EW}_{Pa\gamma}$	$F_{Pa\gamma}$	$\Delta F_{Pa\gamma}$	$L_{Pa\gamma}$	$\Delta L_{Pa\gamma}$
G010.8411-02.5919						
G010.8856+00.1221						
G012.9090-00.2607						
G014.9958-00.6732						
G015.1288-00.6717	-0.8	0.3	4.7E-19	1.8E-19	1.0E+00	3.9E-01
G017.6380+00.1566						
G018.3412+00.1566						
G023.3891+00.1851						
G025.4118+00.1052A						
G026.2020+00.2262						
G026.3819+01.4057						
G027.7571+00.0500						
G029.8620-00.0444						
G030.1981-00.1691						
G033.3891+00.1989						
G033.5237+00.0198						
G034.0500-00.2977_A	9.5	4.1	4.6E-17	2.0E-17	1.1E+00	4.7E-01
G034.0500-00.2977_B	4.2	1.8	1.3E-17	5.5E-18	2.3E+00	1.0E+00
G034.7123-00.5946						
G056.4120-00.0277	-7.6	3.0	8.4E-18	3.3E-18	6.3E-01	2.4E-01
G073.6525+00.1944						
G073.6952-00.9996						
G076.3829-00.6210	-12.4	4.8	5.5E-17	2.1E-17	2.0E+01	7.8E+00
G077.4622+01.7600						
G078.8867+00.7087						
G094.3228-00.1671						
G094.6028-01.7966	-14.1	6.0	7.1E-17	3.0E-17	3.8E+00	1.5E+00
G102.3533+03.6360						
G106.7968+05.3121						
G110.1082+00.0473B_A						
G110.1082+00.0473B_B	1.8	0.7	1.5E-17	5.7E-18	3.5E-01	1.4E-01
G111.2348-01.2385						
G111.5234+00.8004A	-8.4	3.3	2.8E-17	1.1E-17	1.0E+03	3.9E+02
G111.5423+00.7776						
G120.1483+03.3745	-24.2	9.4	4.0E-17	1.6E-17	1.1E+04	4.2E+03
G151.6120-00.4575	-9.3	3.6	6.8E-17	2.7E-17	1.7E+03	6.8E+02
G213.7040-12.5971_A						
G213.7040-12.5971_B						
G233.8306-00.1803A						

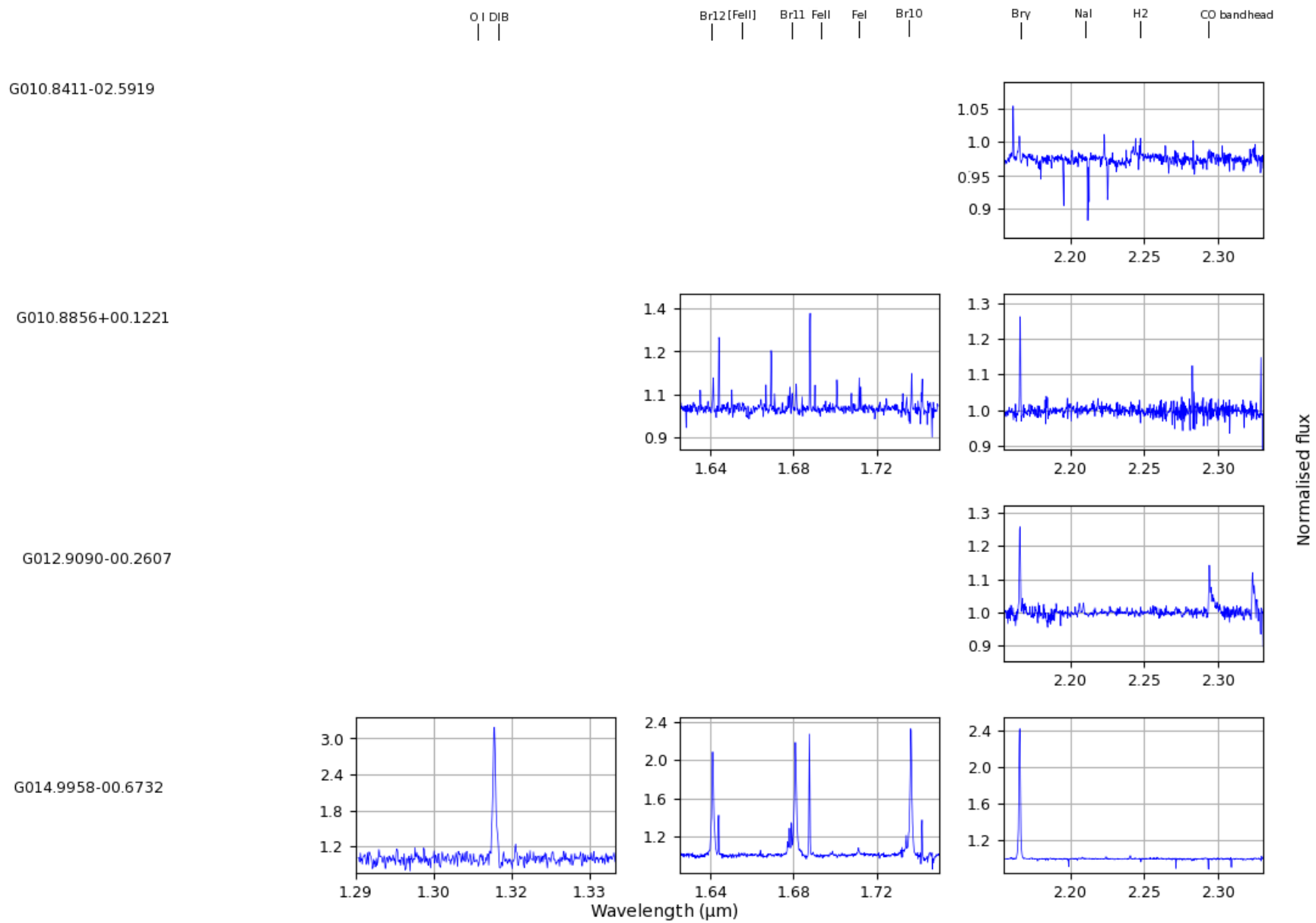


**Figure 1.** Continuum normalised spectra, with left to right panels showing X, J, H and K bands

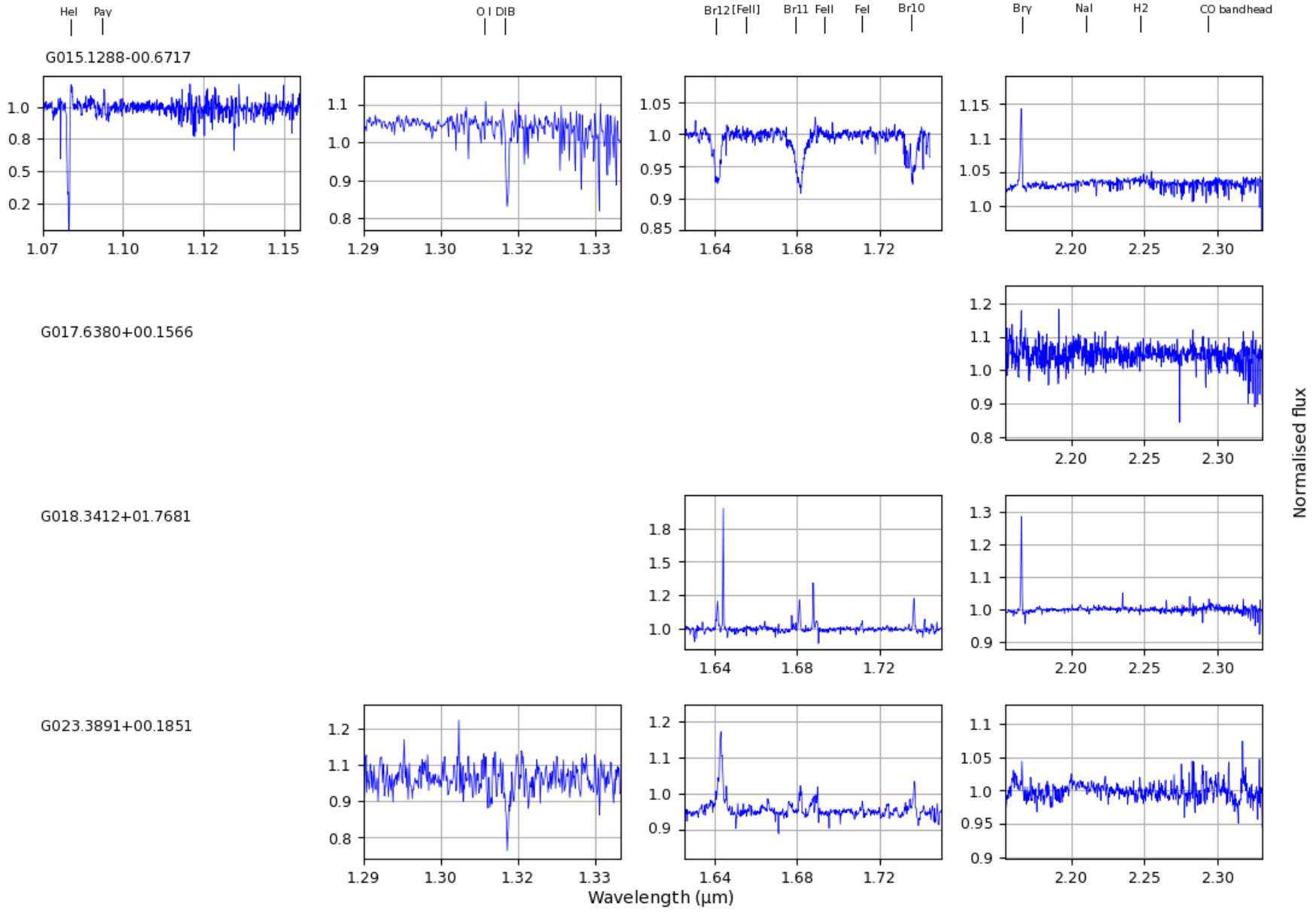


**Figure 2.** Continuum normalised spectra, with left to right panels showing X, J, H and K bands

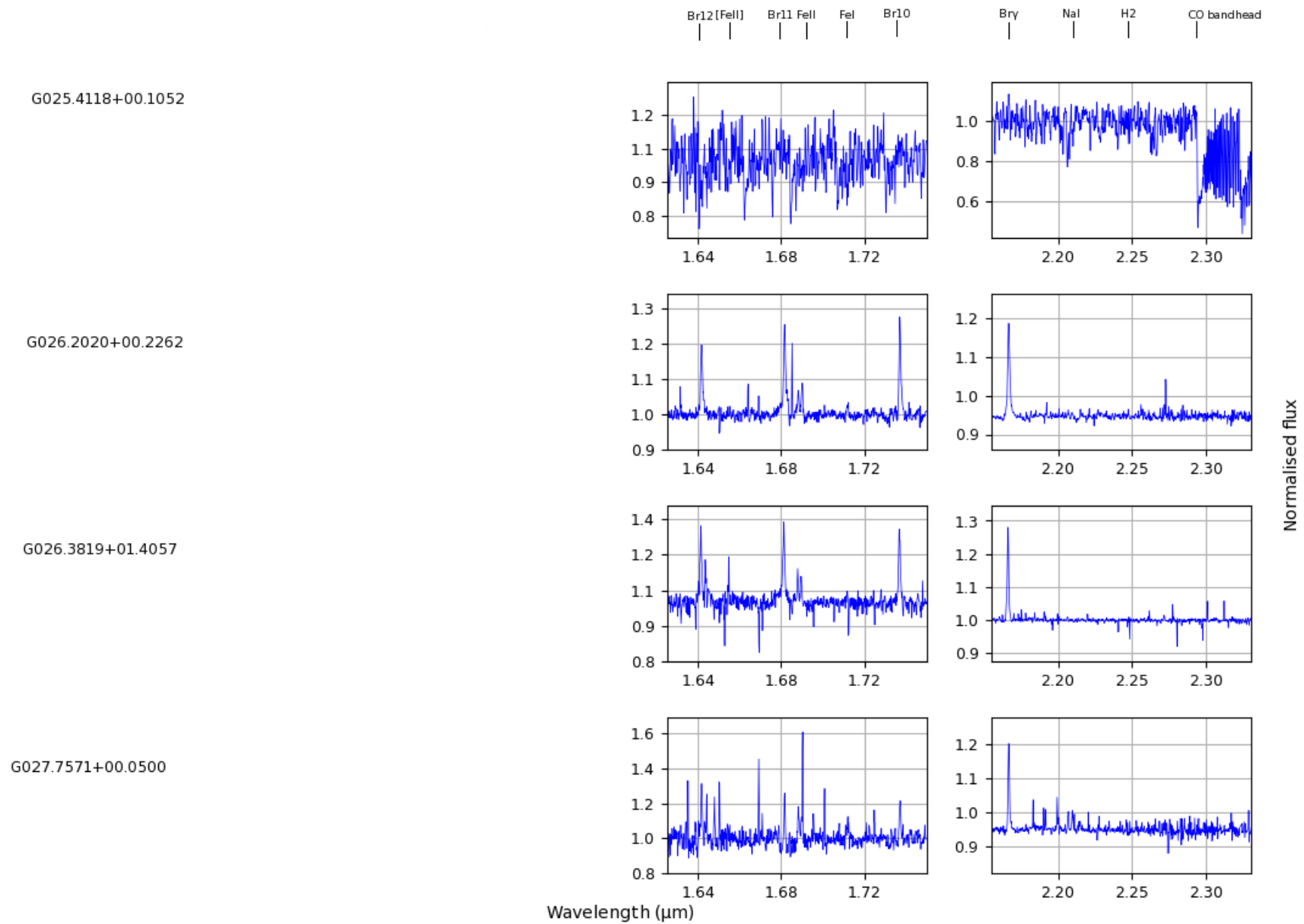


**Figure 3.** Continuum normalised spectra, with left to right panels showing X, J, H and K bands

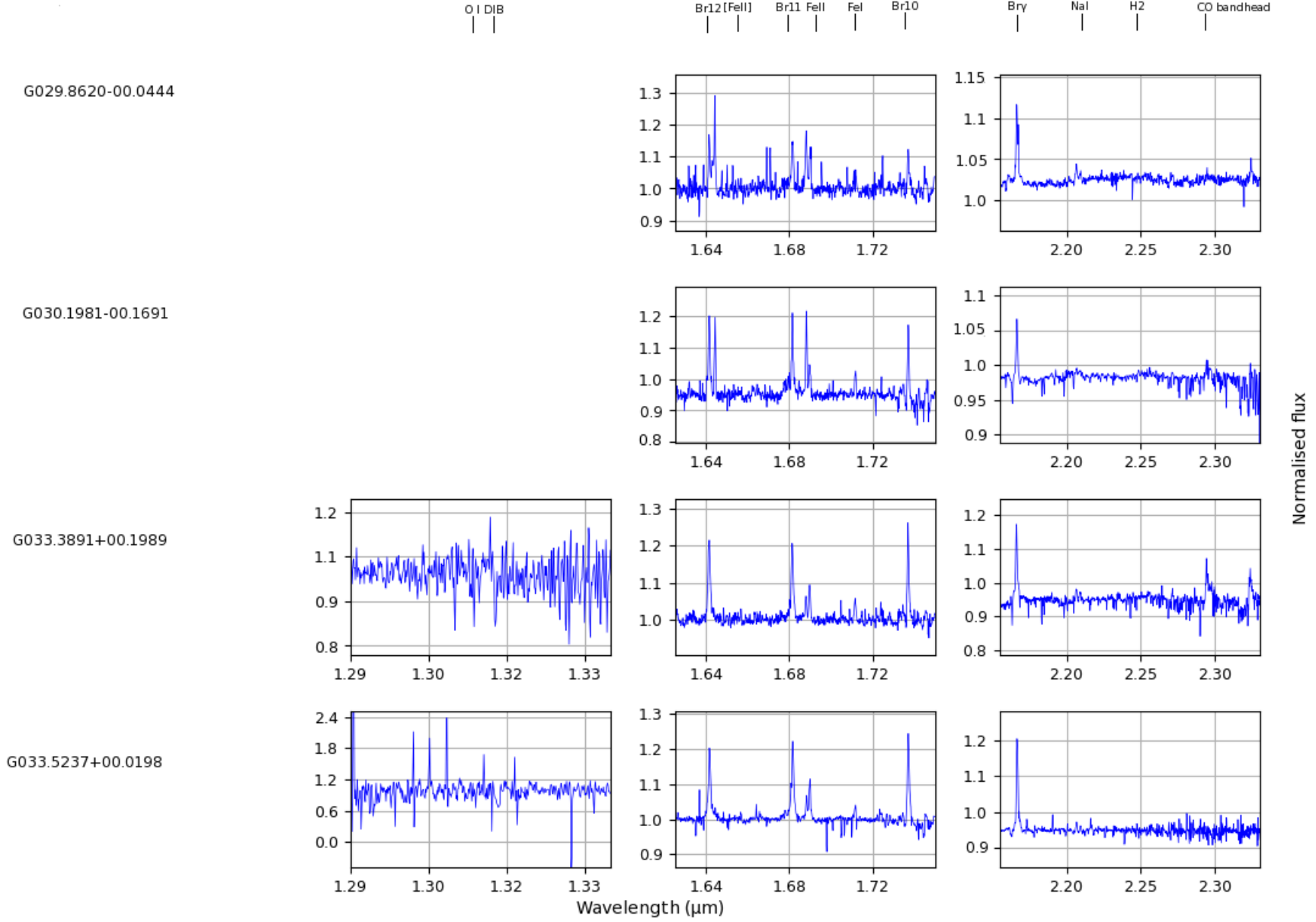


**Figure 4.** Continuum normalised spectra, with left to right panels showing X, J, H and K bands

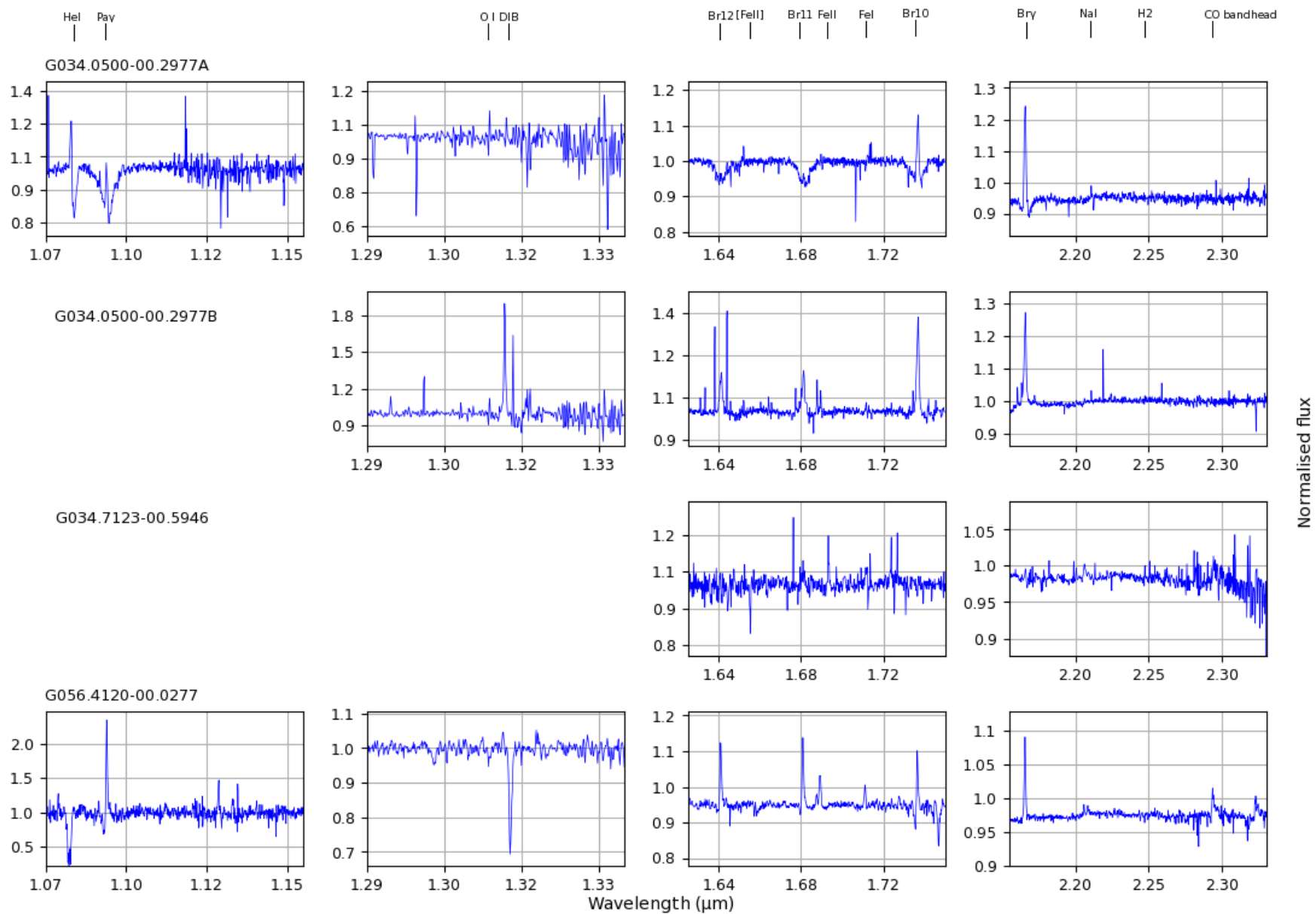


**Figure 5.** Continuum normalised spectra, with left to right panels showing X, J, H and K bands

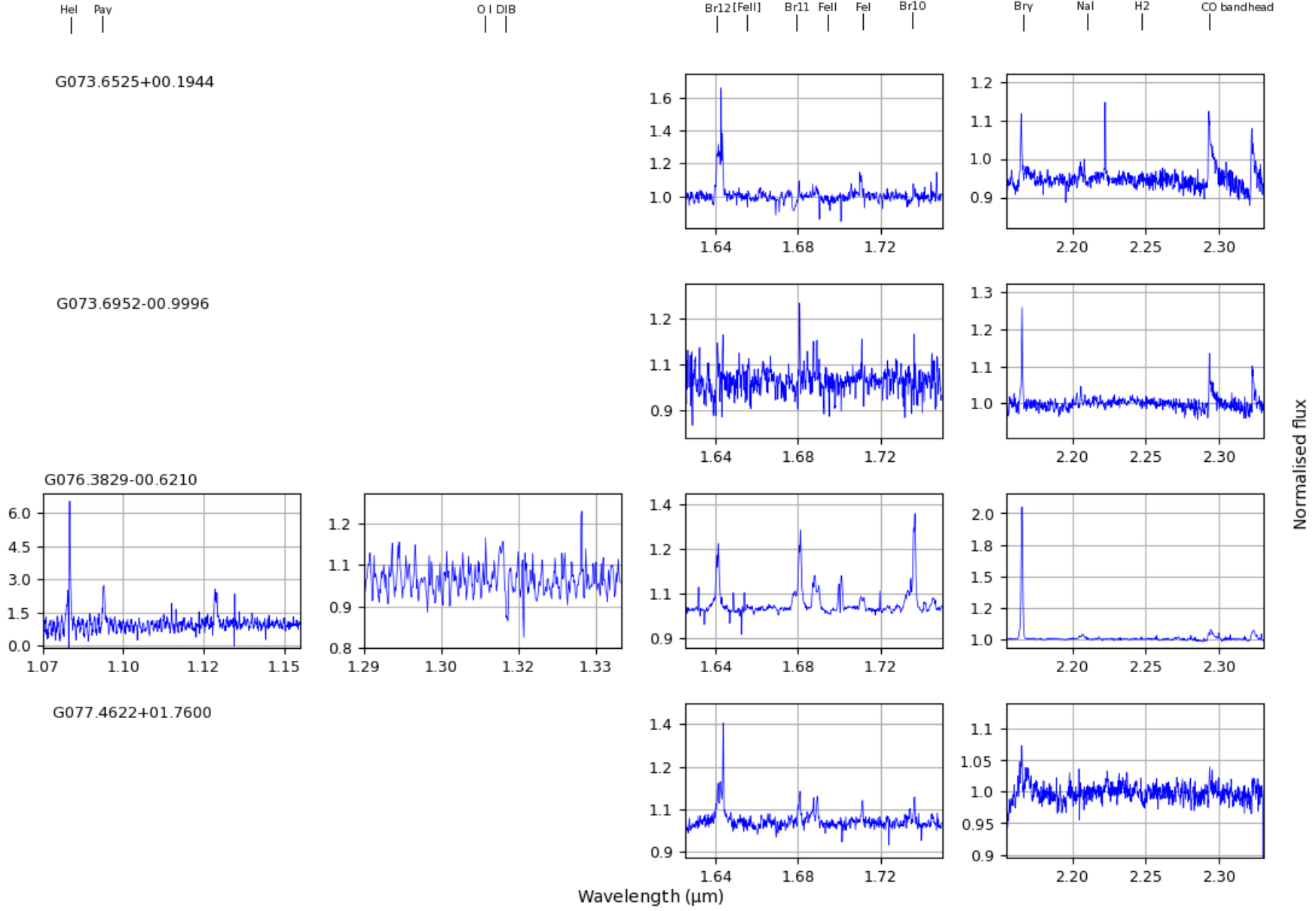


**Figure 6.** Continuum normalised spectra, with left to right panels showing X,J,H and K bands

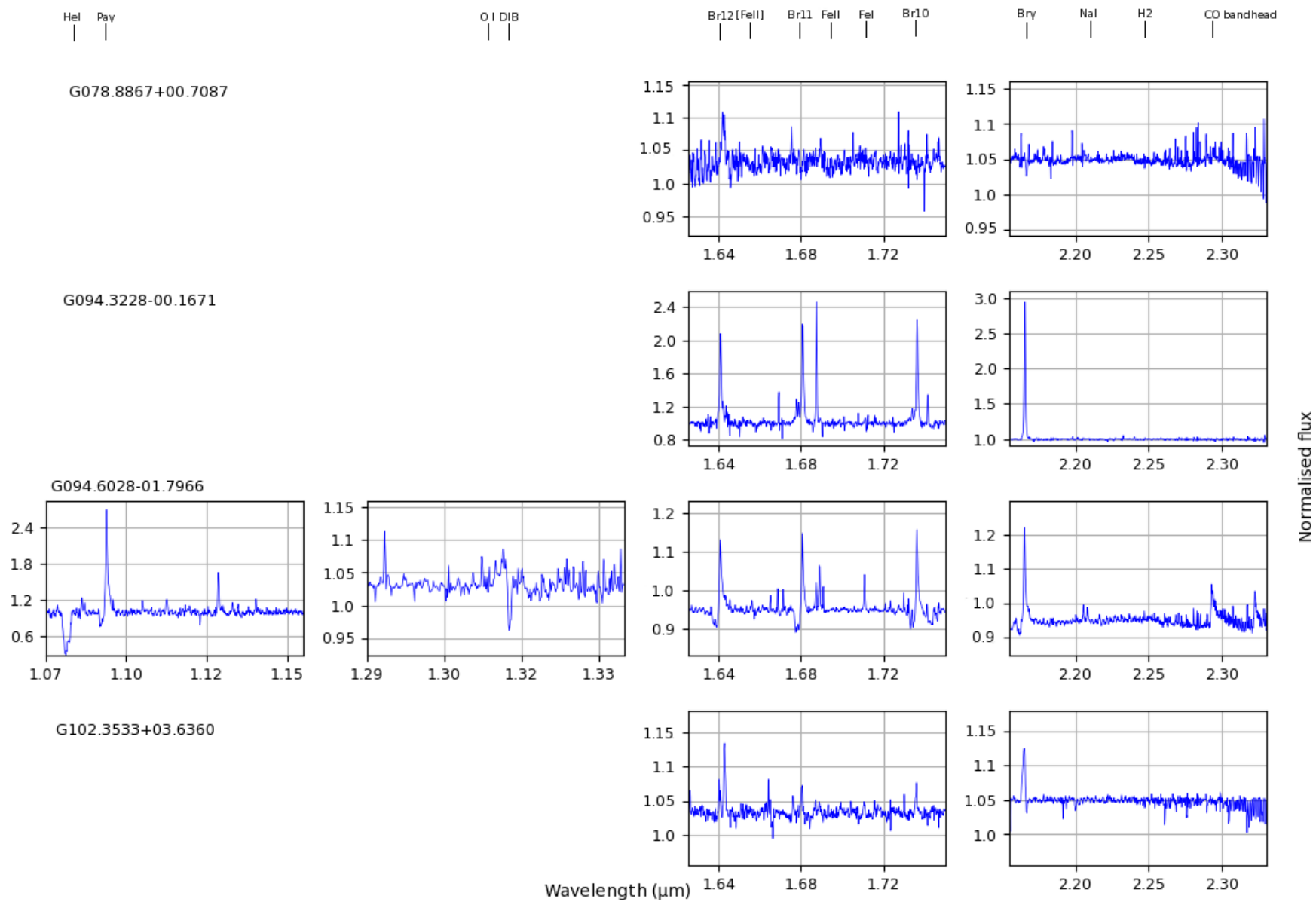


**Figure 7.** Continuum normalised spectra, with left to right panels showing X, J, H and K bands

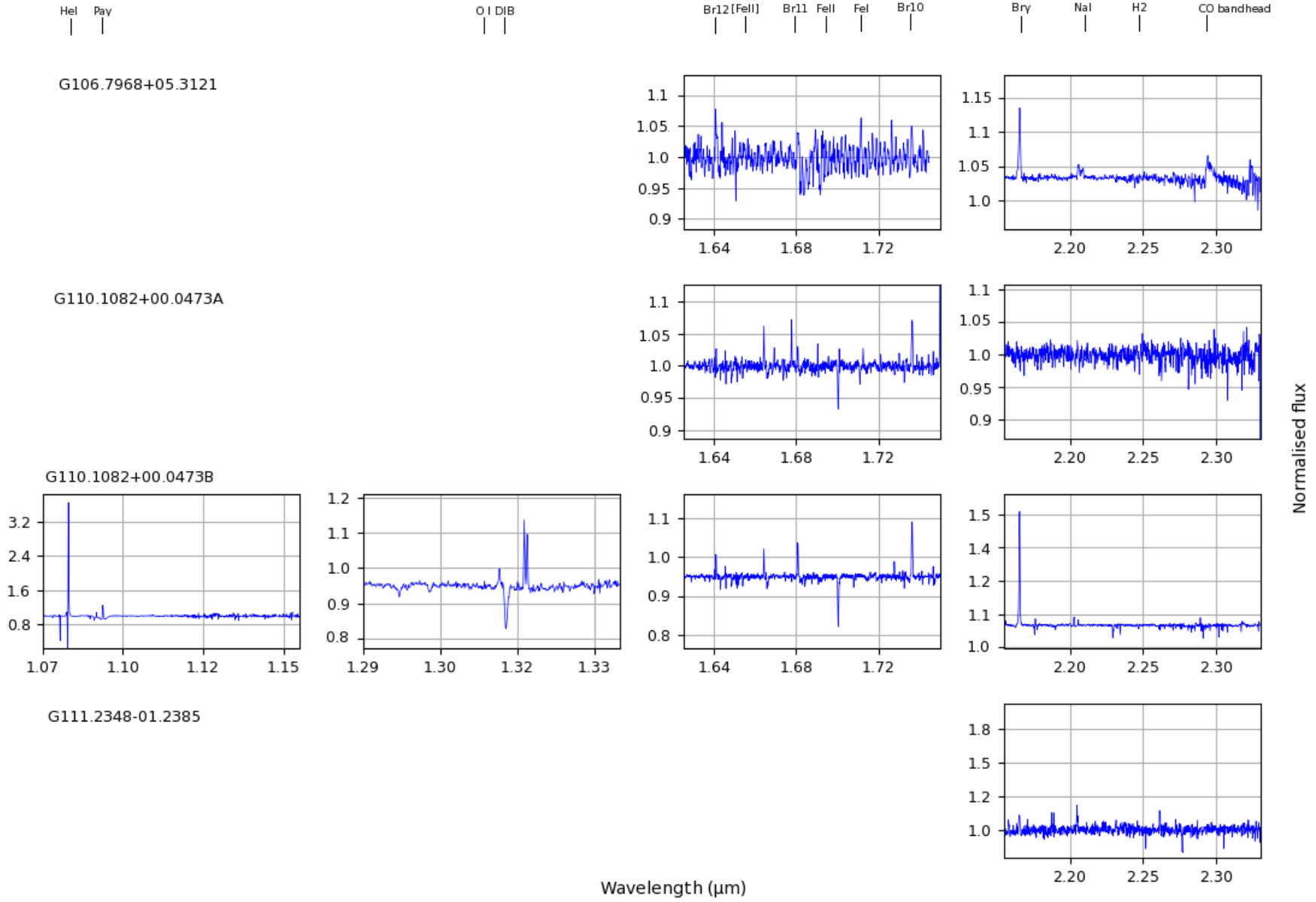


**Figure 8.** Continuum normalised spectra, with left to right panels showing X,J,H and K bands

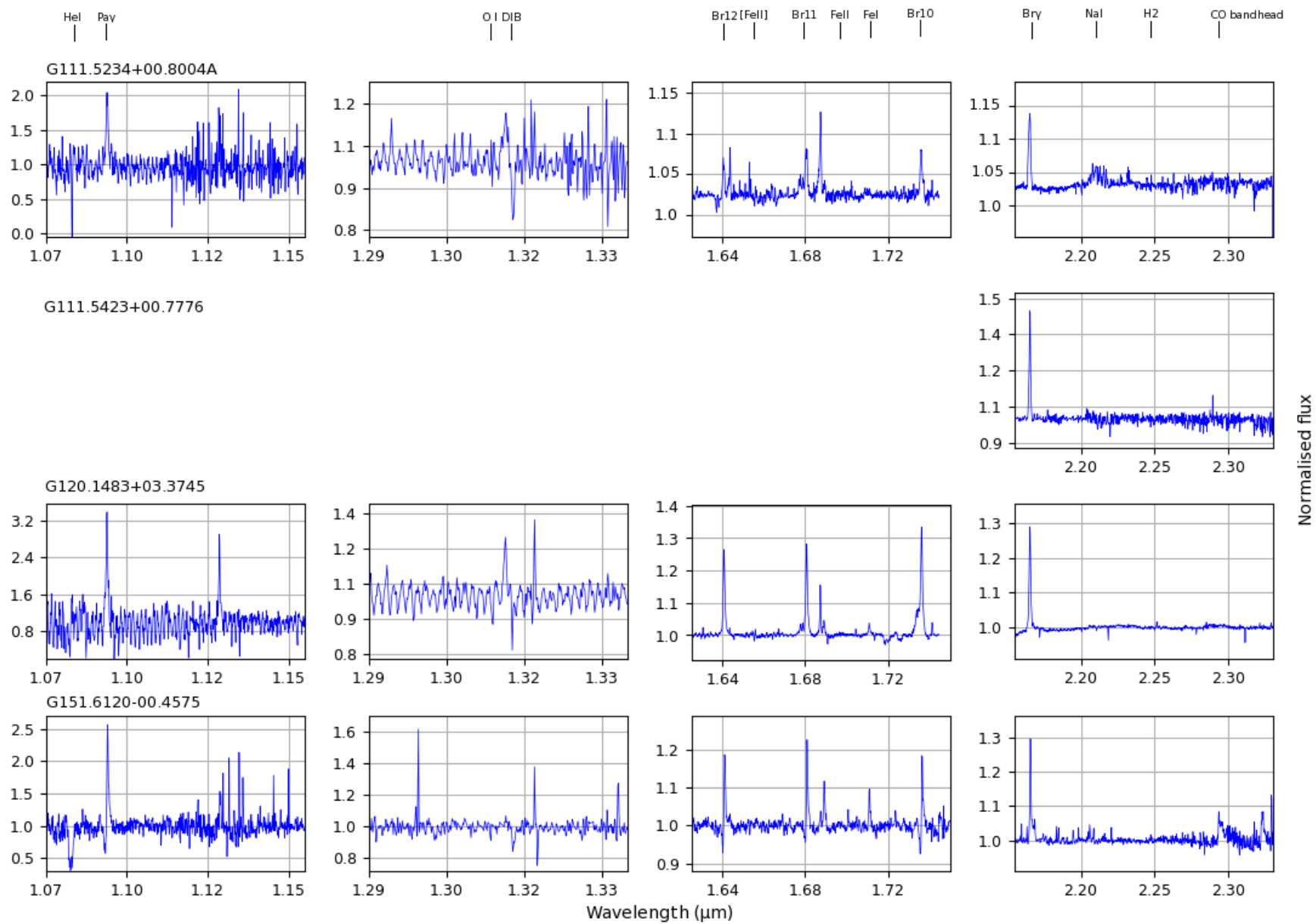


**Figure 9.** Continuum normalised spectra, with left to right panels showing X, J, H and K bands

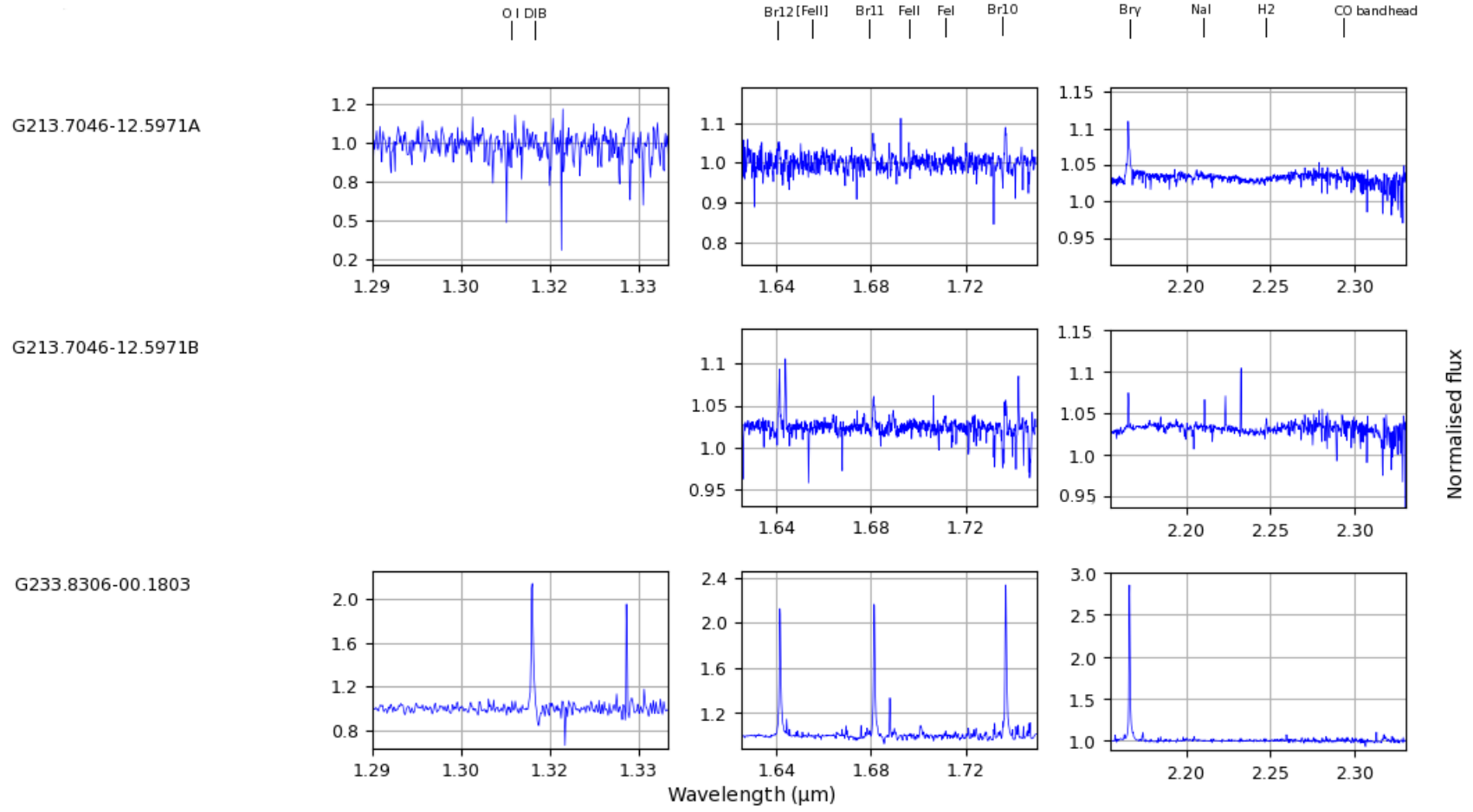


**Figure 10.** Continuum normalised spectra, with left to right panels showing X, J, H and K bands